M. Babaiasl, S. Boccelli, Y. Chen, F. Yang, J.-L. Ding, J.P. Swensen
Predictive Mechanics-Based Model for Depth of Cut (DOC) of Waterjet in Soft Tissue for Waterjet-Assisted Medical Applications
Medical & Biological Engineering & Computing, Vol. 58, N. 8, 2020, p. 1845-1872
doi:10.1007/s11517-020-02182-0

Predictive Mechanics-based Model for Depth-of-Cut (DOC) of Waterjet in Soft-Tissue for Waterjet-assisted Medical Applications

Mahdieh Babaiasl · Stefano Boccelli · Yao Chen · Fan Yang · Jow-Lian Ding · John P. Swensen

Received: date / Accepted: date

Abstract The use of waterjet technology is now prevalent in medical applications including surgery, soft tissue resection, bone cutting, waterjet steerable needles, and wound debridement. The depth of the cut (DOC) of a waterjet in

Mahdieh Babaiasl
M3 Robotics Lab
School of Mechanical and Materials Engineering
Washington State University
Pullman, WA, 99163
E-mail: mahdieh.babaiasl@wsu.edu

Stefano Boccelli
Department of Aerospace Science and Technology
Politecnico di Milano
Milan, Italy, 20156
E-mail: stefano.boccelli@polimi.it

Yao Chen
School of Mechanical and Materials Engineering
Washington State University
Pullman, WA, 99163
E-mail: yao.chen@wsu.edu

Fan Yang
School of Mechanical and Materials Engineering
Washington State University
Pullman, WA, 99163
E-mail: fan.yang6@wsu.edu

Jow-Lian Ding
School of Mechanical and Materials Engineering
Washington State University
Pullman, WA, 99163
E-mail: jowlian_ding@wsu.edu

John P. Swensen
School of Mechanical and Materials Engineering
Washington State University
Pullman, WA, 99163
E-mail: john.swensen@wsu.edu

soft tissue is an important parameter that should be predicted in these applications. For instance, for waterjet-assisted surgery, selective cutting of tissue layers is a must to avoid damage to deeper tissue layers. For our proposed fracture-directed waterjet steerable needles, predicting the cut-depth of the waterjet in soft tissue is important to develop an accurate motion model, as well as control algorithms for this class of steerable needles. To date, most of the proposed models are only valid in the conditions of the experiments and if the soft tissue or the system properties change, the models will become invalid. The model proposed in this paper is formulated to allow for variation in parameters related to both the waterjet geometry and the tissue. In this paper, first the cut-depths of waterjet in soft tissue simulants are measured experimentally, and the effect of tissue stiffness, waterjet velocity, and nozzle diameter are studied on DOC. Then, a model based on the properties of the tissue and the waterjet is proposed to predict the DOC of waterjet in soft tissue. In order to verify the model, soft tissue properties (constitutive response, and fracture toughness) are measured using low strain rate compression tests, Split-Hopkinson-Pressure-Bar (SHPB) tests, and fracture toughness tests. The results show that the proposed model can predict the DOC of waterjet in soft tissue with acceptable accuracy if the tissue and waterjet properties are known.

Keywords depth-of-cut · waterjet · fracture mechanics · Ogden model · waterjet-assisted surgery · steerable needles

1 Introduction

The use of waterjets in strong solids has been used for decades in manufacturing and machining. Models have already been developed for depth of cut of waterjet in strong solids [26], [61], [63], [62], [18], [42], and [60]. Wang *et al.* [61] developed a predictive model for depth of cut of abrasive waterjet in alumina ceramics using a dimensional analysis technique. Other researchers used solid particle erosive theories [63], an energy conservation approach [62], fracture mechanics [18], and dimensional analysis [60] to predict the DOC of waterjet in hard solids. In all of these models, the constants are found by cutting tests, so they are mostly dependent on the experiments. On the other hand, the models developed for strong solids are not applicable to soft solids since the penetration mechanism into the strong solid is different from that of the soft tissue [53].

Recently, waterjets have been used as a surgical tool in waterjet-assisted surgery [9,33,65,45,38,37,52,23,64,3,59,48,58,44,39]. Shi *et al.*[56] has described many advantages that waterjet cutting has over similar approaches to tissue cutting. Waterjet have also been used to drill holes in bones [17,16, 24]. The mechanism of cutting in these applications is through delivering the kinetic energy of the high-velocity waterjet coming out of a sub-millimeter nozzle to the intended tissue. In these applications, predicting the DOC of waterjet in soft tissue is a necessity for selective tissue cutting in order to avoid damage to deeper layers.

Oertel *et al.* [38] used a waterjet device called Helix Hydro-Jet (Erbe, Tubingen, Germany) to dissect the brain parenchyma. They showed that the waterjet allows for accurate, precise, and reliable dissection of the porcine cadaver brain while preserving the vessels by controlling waterjet pressure. They experimentally showed that there is a linear relationship between the waterjet pressure, and depth of dissection. Therefore, the Erbe devices provide manual control of the depth of cut by manually adjusting the waterjet pressure.

Yamada *et al.* [65] used pulsed waterjet to dissect swine livers. They have evaluated the depth of dissection using light microscopy and histology. They experimentally concluded that the depth of dissection has a direct relationship with the velocity of the waterjet, and an inverse relationship with the breaking strength of the liver parenchyma. In their study, no predictive model for DOC is proposed. Furthermore, the mechanical properties of the soft tissue were measured at a penetration rate of $1\frac{mm}{s}$ that is not comparable to the penetration rate of the high-velocity waterjet. Morad *et al.* [33] tried to control the cut depth of waterjet surgical device by controlling the pressure of waterjet; however they stated that while using the waterjet surgical device there is a risk of cutting unwanted tissue layers. They proposed to experimentally tune DOC based on the applied pressure; however they left this to a future study.

The Erbejet device [56,58] is a waterjet device that allows for tissue-selective cutting based on a pre-selected pressure. The pressure range with a 120 μm nozzle for this device is $1-8$ MPa with a volumetric flow rate of $1-55\ \frac{ml}{min}$. For this device, also, the depth of cut is controlled by controlling pressure, and no closed-loop control system is available to control the cut-depth.

Predicting DOC of liquid in soft tissue is also important from needle-free drug injections point of view [32,35]. In these devices, the desired drug is ejected from a nozzle of diameter in the range of 30 to 560 μm at a velocity of $\approx 100\frac{m}{s}$ [47]. It is important to know how deep the drug has penetrated into the soft tissue using a jet injector to ensure the efficacy of the treatment. In the literature, some researchers studied the penetration characteristics of these devices [11,49,50]. These studies experimentally showed that the jet penetration is a function of injected volume of drug, jet velocity, nozzle diameter, and stiffness of the penetrated soft solid.

Microjet injection devices inject small amounts of drug in a repetitive way [2,47]. Romhens *et al.* [47] studied the effect of velocity of the microjet on its penetration capacity using a repetitive microjet injection device. They experimentally concluded that microjects with over $90\frac{m}{s}$ velocity can penetrate epidermal skin sample, and their study does not lead to a predictive model for depth of penetration of microject into the skin. The diameter of the microjets are 50 μm each.

Morad *et al.* [34] developed a waterjet cutting probe for flexible surgical robot to excise cancerous tissue from the spine. They experimentally studied the effect of tissue and waterjet properties on cut depth. They concluded that the depth of cut has a direct relationship with waterjet pressure, and the duration of the application of waterjet but has an inverse relationship with

modulus of elasticity of the soft tissue. They also mentioned that although waterjet cutting provides many advantages compared to traditional methods, however there is a risk of jet cutting through the soft tissue and going to underlying tissues, and damaging them. Thus, this necessitates an approach to predict the depth of cut based on the waterjet and soft tissue properties.

Schramm-Baxter *et al.* [50] developed a simple model based on fluid dynamics to predict the penetration depth as a function of centerline velocity. In another study, Schramm-Baxter *et al.* [49] proposed a lumped parameter called exit jet power P_{jet} that collects all the jet parameters including diameter, and velocity into one parameter to study the jet mechanics. They showed that the jet penetration depth increases with increasing jet power up to some point. Their proposed models are oversimplified, and are far from the real penetration situation. For instance, in their models, the surrounding soft tissue is considered to be fluid and its effects are described by a lumped parameter of critical stress.

Different empirical models are proposed in the literature for the penetration depth of the liquid jet in soft solid. Baxter *et al.* [11] developed an empirical model based on a critical stress, and centerline velocity for turbulent jet flows. Tagawa *et al.* [57] proposed a viscous stress model based on the stress at the wall of the hole formed by liquid jet. Thus resulting in a simple model for the depth of penetration as a function of velocity, and time. This model provides a reasonable prediction when the duration of the penetration is small enough. For longer penetration times, the interaction between the soft tissue and the liquid jet is significant. At the beginning, the penetrating jet must be powerful enough to puncture the surface, and then provide enough inertial pressure to overcome both the elastic stress of the surrounding soft tissue, and the hydrodynamic stress to penetrate soft tissue. Thus for longer duration penetration, the properties of the soft tissue should also be considered to accurately describe the dynamics of liquid jet penetration into soft tissue.

From this overview of the literature, there is an explicit need for the development of a mechanics, non-heuristic model that can predict the depth of cut as a function of the needle and tissue parameters. This work provided the development and validation of such a model. We demonstrate the use of this model for our lab's application waterjet-assisted steerable needles [8] in which the direction of the tissue fracture is controlled with the waterjet, and then the flexible needle follows. Having a closed-form mathematical relation for depth of cut of waterjet in soft tissue is a necessity to accurately control these devices. In previous research we have developed a finite element model to predict the DOC of waterjet in soft tissue [7]. However, finite element analysis require high computation time and is not suitable from feedback control point of view. This raises the need to have a closed mathematical solution to be embedded in the control software of the waterjet steerable needles. Fig. 1 shows the definition of the DOC of waterjet in soft tissue. The depth of cut of waterjet in soft tissue is dependent on the tissue properties such as shear modulus, strain hardening factor, and fracture toughness as well as waterjet properties such as diameter, and velocity.

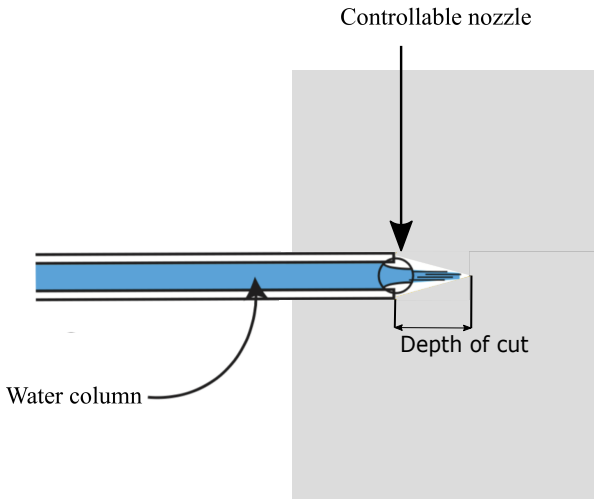

Fig. 1 Definition of DOC of waterjet in soft tissue. Waterjet cuts a small path in front of the nozzle, and the length of this path is dependent on the tissue properties (constitutive response, and fracture toughness) as well as waterjet properties (diameter, and velocity).

In this paper, a physics-based model to predict the DOC of waterjet in soft-tissue is proposed for waterjet-assisted medical applications. This model is based on fracture mechanics and is a function of tissue properties such as fracture toughness and shear modulus, as well as waterjet properties such as diameter and velocity. The model is validated using the mechanical properties of SEBS soft tissue simulants. Tissue properties are measured at the corresponding strain rates associated with waterjet cutting of soft tissue. SEBS is chosen as the main material for soft tissue simulants whose viscoelastic nature makes it a good candidate as a substitute for real biological tissues [36]. On the other hand, these soft tissue simulants are optically clear, have better durability due to non-aqueous solvents, and their mechanical properties are easily changed to study the wide range of potential tissue properties. Characterization of the SEBS soft tissue simulants are done using static compression tests, SHPB tests, and fracture toughness tests. These tests are modified from their traditional forms to fit the challenging tests on soft materials.

The experimental data for this paper along with codes to run the data are uploaded to Mendeley Data in order for other researchers to use them for their own research purposes. The experimental data for depth of cut are available at (`http://dx.doi.org/10.17632/zvdrpzmkcb.2`), the data for Static compression tests are available at (`http://dx.doi.org/10.17632/gswfx544cs.3`), and the data for SHPB tests are available at (`http://dx.doi.org/10.17632/`

msvjxfh7nh.1). Videos of the waterjet cutting soft tissue during experiments can be found here.

2 Materials and Methods

In this section, the material and methodology used for soft tissue preparation, tests to characterize tissue properties, experimental setup used for experiments, and mathematical description of the predictive mechanics-based model for depth-of-cut (DOC) are described.

2.1 Soft Tissue Simulant Preparation

Because of the challenges related to using, storing, and imaging of real biological tissues, different substitute materials as soft tissue simulants are used by researchers around the world for experiments [36], [4], [31], [46], and [30]. These tissue-mimicking phantoms give an average approximation of the soft tissue. Common materials used in tissue mimicking simulants are Gelatin, rubber, leather, silicone elastomers, PVA, and lard. The mechanical properties of water-based tissue mimicking simulants such as Gelatin, and PVA are variable with respect to time, temperature, and humidity.

Because of the mentioned difficulties in common tissue mimicking simulants, we have used Poly (styrene-b-ethylene-co-butylene-b-styrene) triblock copolymer (SEBS), Kraton Polymers LLC (G1650, and G1652, Houston, TX, USA) as the main material for our tissue-mimicking simulants [36], [19], and [20]. The solvent used for SEBS is light mineral oil, which makes it a more environmentally stable substitute for water-based hydrogels. This increases its operational temperature ranges, and storage life. Soft tissue simulants that are made of SEBS are optically clear. This feature is desirable from imaging point of view. So, optical cameras can be used instead of pricey imaging devices to see what is going on inside the soft tissue during experiments. A wide range of tissue stiffnesses can be studied by simply changing the ratio of polymer content to mineral oil. In comparison to silicone rubbers, SEBS has also low friction due to its oil solvent.

To make the tissue simulants, SEBS material and mineral oil are weighed out to produce mixtures with 10, 15, and 20 vol% SEBS. To calculate the necessary weight, the densities of SEBS, and mineral oil are considered to be $\rho_{SEBS} = 0.91\frac{g}{cm^3}$, and $\rho_{oil} = 0.85\frac{g}{cm^3}$, respectively. Then the mass of the required material can be calculated using $m = \rho V$, in which m, ρ, and V are required mass of the material (either SEBS or mineral oil), density (SEBS or mineral oil), and volume of the material (SEBS or mineral oil).The mixture is then put in the oven at 150^oC for about 2 to 8 hours based on the percentage of SEBS, and it was mixed from time to time to get a homogeneous solution without any undissolved powder. After this time, the solution is degassed using a vacuum pump with a chamber to put SEBS to eliminate any air bubbles

trapped in the solution. The solution is then poured into molds of desired dimensions based on the experiment to be conducted, and then let cool down to room temperature and solidify before releasing from the molds.

For depth of cut experiments, custom-designed acrylic rectangular molds of dimensions $100 \times 100 \times 30$ mm are used. For, static compression tests, 3D printed molds of cylindrical shape are used to get the final tissues with diameter of 25 mm, and heights of 10 mm. For high strain rate tests conducted with Split Hopkinson Pressure Bar (SHPB) setup, custom-designed 3D printed-Acrylic molds of rectangular shape with thickness of 2 mm is used and then punches with diameter of 10 mm are utilized to cut cylindrical samples out of the rectangular tissue yielding cylindrical samples of diameter 10 mm with thickness of 2 mm. Finally, for fracture toughness tests, custom-designed 3D printed ABS-Acrylic sheet mold was used to cast long taper shaped samples with thickness of $4mm$ at the center and a height of $15mm$. Then the samples are cut into specimens with length of $50mm$. Fig. 2 show the custom-designed molds, and resultant tissues for depth of cut experiments, static compression tests, SHPB tests, and fracture toughness tests.

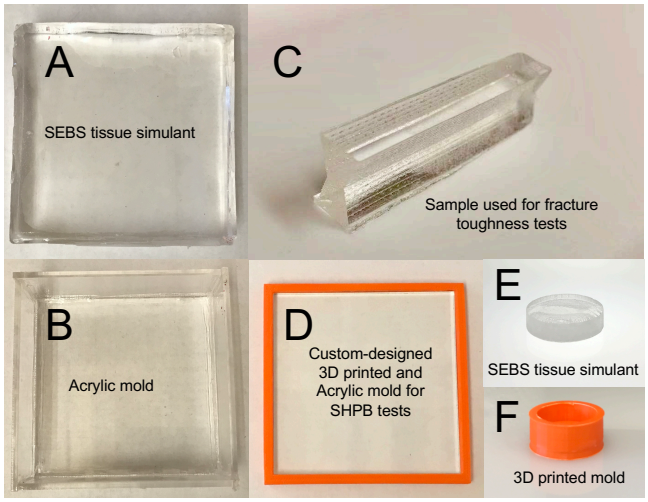

Fig. 2 Custom designed molds and resultant tissues used for cut-depth experiments, static compression tests, SHPB tests, and fracture toughness tests. (A, and B) SEBS tissue simulant used for DOC experiments and Acrylic mold of $100 \times 100 \times 30$ mm dimensions. (C) Resultant tissue used for fracture toughness tests. (D) Acrylic-3D printed mold of thickness 2 mm to make tissues for SHPB tests. 10 mm punch is used to cut cylindrical samples for SHPB tests. (E, and F) SEBS tissue simulant, and custom-designed 3D printed mold of diameter 25 mm and height of 10 mm used for static compression tests. (images not to scale)

2.2 Low Strain Rate Static Compression, High Strain Rate Split-Hopkinson-Pressure-Bar (SHPB), and Fracture Toughness Tests on SEBS Soft Tissue Simulants

According to our compression tests at low rates of strain as well as tensile, compression, and rheological tests conducted in [36] at lower rates of strain, the material properties of SEBS is not dependent on low and medium rates of strain. Thus, in order to find the shear modulus at higher rates of strain, the data from SHPB tests are extrapolated to higher rates of strain.

The quasi-static tests are performed with an Instron 600DX machine controlled by Bluehill 3 software. The samples are compressed between metal plates with constant strain rates of 0.001, 0.01, and 0.1 s^{-1}. The change of gauge length is measured with the build-in function of the Instron machine, and the force is measured by a 25lb load cell. The engineering strain can be calculated by:

$$\varepsilon = \frac{\Delta L}{L_0} \tag{1}$$

where ΔL is the thickness, and L_0 is the initial length of the specimen. The engineering stress can be calculated by:

$$\sigma = \frac{F}{A_0} \tag{2}$$

where F is the force applied, and $A_0 = \frac{\pi {D_0}^2}{4}$, with D_0 being the initial diameter, is the initial cross sectional area of the sample.

The high strain rate tests were conducted with Split-Hopkinson-Pressure-Bar (SHPB) adapted for soft materials. Fig. 3 is a schematic of the SHPB setup, which consists of a striker, an incident bar, a transmitted bar and a buffer. The specimen is sandwiched between the incident bar and transmitted bar. When the striker impacts the free end of incident bar, a compressive stress pulse is generated at the impact surface and propagate along the incident bar. When the incident wave reaches the specimen, part of the wave transmits through the specimen and propagates into the transmitted bar, and the other part is reflected to the incident bar. The strains generated by passing waves are recorded by the strain gauges attached to the bars as ε_I, ε_T, and ε_R for incident, transmitted, and reflected waves, respectively. The strain rate of the specimen can be calculated by:

$$\dot{\varepsilon}_s(t) = -\frac{2c_b}{L_0}\varepsilon_R(t) \tag{3}$$

where $c_b = \sqrt{E_b/\rho_b}$ is the longitudinal sound speed of the bar material, with E_b and ρ_b being the elastic modulus and density of the bar material, respectively. The engineering strain of the specimen can be calculated by:

$$\varepsilon_s(t) = \int_0^t \dot{\varepsilon}_s(t)dt \tag{4}$$

and the engineering stress is calculated by:

$$\sigma_s(t) = \frac{E_b A_b}{A_0} \varepsilon_T(t) \tag{5}$$

where A_b is the cross-sectional area of the bar and A_0 is the original area of the specimen [22], [13].

In the tests, the striker velocity is adjusted to achieve strain rates in the specimen of 3000, 4500, and 6000 s^{-1}. More details about these tests are included in a separate paper in progress.

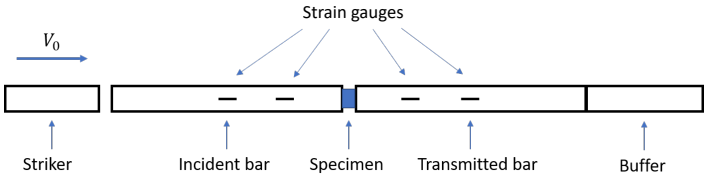

Fig. 3 Schematic of the SHPB test setup. The SHPB consist of a striker, and incident bar, a transmitted bar, and a buffer. The bars are adjusted for soft tissue experiments, and the material used for the bars is PEEK.

Fracture toughness is measured with trouser tear test. An initial notch is cut on the centerline of the specimen, then the two arms are fixed with two 3D printed holders that connect to the Instron machine as shown in Fig. 4. During the tests, the specimen is pulled vertically at constant speeds of 0.1, 0.5, and 1 $\frac{mm}{s}$. The load is measured with a 1 kg load cell. The fracture toughness can be calculated by:

$$J = \frac{F_{ave}}{2w} \tag{6}$$

Where F_{ave} is the average force during the crack growth and w is the width of the specimen [67].

In order to predict the constitutive response of the tissue in static compression, and SHPB tests, Ogden model [40] presented in 24 is used. This strain energy per undeformed unit volume function describes the constitutive response of an incompressible, isotropic, and hyperelastic solid. Research showed that strain hardening factor α is constant with strain rate, and only the shear modulus changes with strain rate [55]. Therefore we adopted α from fitting stress strain data at strain rate of $\dot{\varepsilon} = 0.01/s$ with Ogden model. When α is found at this strain rate, it is held constant for other strain rates so that only shear modulus μ varies with strain rate. In order to fit the data with Ogden model and evaluate constants μ (shear modulus), and α (strain hardening factor), the following procedure is adopted.

Fig. 4 Schematic of the experimental setup to measure the fracture toughness of the SEBS soft tissue simulants. Trouser tear test is used to measure the fracture toughness of the SEBS soft tissue simulants to mode I crack propagation.

In short, the nominal stress in the direction of the applied load is predicted using Ogden model and then it is compared to the measured nominal stress during tests. By definition, one can write:

$$\sigma_i = \frac{d\phi}{d\lambda_i} \tag{7}$$

Where, σ_i are principal stresses associated with principal stretch ratios λ_i $(i = 1, 2, 3)$. With the assumption that the tissue sample is at the state of plane stress during the compression tests, $\sigma_x = \sigma_y = 0$ holds (suppose a Cartesian coordinate system where the z-axis is aligned with the direction of load applied during the test). In this paper, soft solid is considered to be incompressible. Therefore, from conservation of volume, one can conclude $\lambda_x \lambda_y \lambda_z = 1$ for the principal stretch ratios. Therefore $\lambda_x = \lambda_y = \frac{1}{\sqrt{\lambda_z}}$. From (24), (7), and the relationship between principal stretch ratios, it is easy to deduct a relationship for σ_z as follows:

$$\sigma_z = \frac{d\phi}{d\lambda_z} = \frac{2\mu}{\alpha}[{\lambda_z}^{\alpha-1} - {\lambda_z}^{-1-\frac{\alpha}{2}}] \tag{8}$$

Therefore the optimization problem is finding values for μ, and α such that the error between the measured (from compression tests) and calculated stress (or nominal stress) is minimized. In order to solve this problem, *lsqcurvefit* function from the Optimization Toolbox of MATLAB is used which solves

nonlinear data-fitting problems in least-squares sense. Trust-region-reflective method is used as the option for the descent algorithm.

As mentioned before, α is not strain rate dependent, however, shear modulus μ varies with strain rate. In waterjet cutting of soft tissue, the velocity of waterjet determines the strain rate. To find the strain rate $\dot{\varepsilon}$ relevant to waterjet penetration into soft tissue, it is assumed that the tissue is strained perpendicular to the penetration direction. Thus the value of strain can be calculated by the following equation:

$$|\varepsilon| = \left|\frac{\pi D - 2d}{2d}\right| = \left|\frac{\pi}{2}\left(\frac{d}{D}\right)^{-1} - 1\right| \tag{9}$$

Where, D, and d are waterjet diameter and steady state diameter of the crack (that opens to accommodate a waterjet of diameter D). Therefore strain rate can be defined as:

$$|\dot{\varepsilon}| = \frac{|\varepsilon|}{t} = \frac{|\varepsilon|}{\frac{D}{v}} = \left|\frac{v}{D}\left[\frac{\pi}{2}\left(\frac{d}{D}\right)^{-1} - 1\right]\right| \tag{10}$$

In this equation, v is the velocity of the waterjet. For simplicity we assume that $d \approx D$. Therefore strain rate equation can be re-written as:

$$|\dot{\varepsilon}| \approx 0.57\frac{v}{D} \tag{11}$$

Since the pump provides volumetric flow rate Q ($\frac{m^3}{s}$), it is more convenient to re-write the velocity of waterjet in terms of Q. Velocity of waterjet at the nozzle depends on volumetric flow rate of water, as well as diameter of the nozzle, and it can be calculated with the following equation:

$$v = \frac{Q}{A} = \frac{4Q}{\pi D^2} \tag{12}$$

In which A is the area of jet coming out of a nozzle of inner diameter D.

The crack growth rate related to waterjet penetration into soft solid (formation, and advancement of the crack) can be predicted as follows:

$$\dot{r} = \frac{d}{D}(\frac{v}{2}) \tag{13}$$

In which $2r = d$. For simplicity as experiments in literature [54] have already shown, one can take $d \approx D$, so that (13) can be written as $\dot{r} \approx 0.5v$. In which, v is the average velocity of waterjet coming out of a nozzle of diameter D, and d is the steady state crack length after waterjet is turned off. Thus the crack growth rate is approximated to be half of the waterjet velocity.

For the two nozzle diameters, and different volumetric flow rates used in this paper, the corresponding strain rates, and crack growth rates associated with waterjet penetration into soft tissue is reported in Table 1.

Table 1 Strain rates ($\dot{\varepsilon}$), and crack growth rates ($\dot{r}$) associated with waterjet diameters (D), and velocities (v) used in this paper. The values of this table are calculated using (11), and (13). In order to accurately validate the depth of cut model, the tissue properties should be measured at the strain rates, and crack growth rates related to waterjet penetration into soft tissue. Note: waterjet diameters are taken to be the inner diameters of the Nitinol tubes.

$D = 0.32mm$				$D = 0.24mm$			
Q ($\frac{mL}{min}$)	$v(\frac{m}{s})$	$\dot{\varepsilon}(s^{-1})$	$\dot{r}(\frac{m}{s})$	Q ($\frac{mL}{min}$)	$v(\frac{m}{s})$	$\dot{\varepsilon}(s^{-1})$	$\dot{r}(\frac{m}{s})$
20	4.15	7.40×10^3	2.07	20	7.37	1.75×10^4	3.69
30	6.22	1.11×10^4	3.11	30	11.06	2.63×10^4	5.53
40	8.30	1.48×10^4	4.15	40	14.74	3.51×10^4	7.37
50	10.37	1.85×10^4	5.18	50	18.43	4.38×10^4	9.21
60	12.44	2.22×10^4	6.22	60	22.12	5.26×10^4	11.06
70	14.51	2.59×10^4	7.26	70	25.80	6.14×10^4	12.90
80	16.59	2.96×10^4	8.29	80	29.49	7.01×10^4	14.74
90	18.66	3.33×10^4	9.33	90	33.17	7.89×10^4	16.59
100	20.73	3.7×10^4	10.37	100	36.86	8.77×10^4	18.43

2.3 Experimental Setup and Measurement of Depth-Of-Cut (DOC)

The experimental setup used for all experiments is depicted in Fig. 5. A linear actuator is used to drive the needle with the velocity of insertion of $1\frac{mm}{s}$ approximately $1cm$ into the soft tissue simulant. A high pressure pump (PR-class Dual Piston, PR100PFT3D, Scientific Systems Inc., State College, PA, USA) provides a constant volumetric flow rate (up to $100\frac{mL}{min}$) and when run, water-jet needle will cut a channel in front of it in the tissue. After about 30 seconds, the camera takes a photo and the photo will be processed in image processing software to measure the depth of cut of water-jet. The software is developed in Matlab to measure the DOC. The software first loads the image and zooms in the area of interest. Then it asks to select a real world measurement and enter the real value of it for calibration (this is done using the rulers on the lightbox). Then the user will select the area of interest to measure, and the software associates the pixel distance to a real-world measurement. Suction canister, and a vacuum pump are used to collect the water sprayed back during experiments.

For the water-jet needle, first a piece of Nitinol tube is cut to a length of 52.8 mm. Next, the Nitinol tube is soldered inside the copper tube of 45 mm length with inner diameter of $ID = 0.94$ mm, and outer diameter $OD = 1.59$ mm. Finally, the copper tubing is attached to the ferruled reducer and then to the water pump via PEEK tubing ($ID = 1.58$ mm, and $OD = 3.2$ mm). Two needles were manufactured with two different diameters to study the effect of diameter on depth of cut. The first needle has Nitinol tube with $ID = 0.32$ mm, and $OD = 0.58$ mm, and the Nitinol tube of the second needle has $ID = 0.24$ mm, and $OD = 0.33$ mm. Fig. 6 shows the first designed needle (the second needle is the same only with a different diameter Nitinol tube).

To measure the depth of cut of water-jet in SEBS tissue, the pump is turned on with the specific flow rate and the water-jet needle is inserted into soft tissue about 1 cm using the linear actuator and with velocity of insertion of

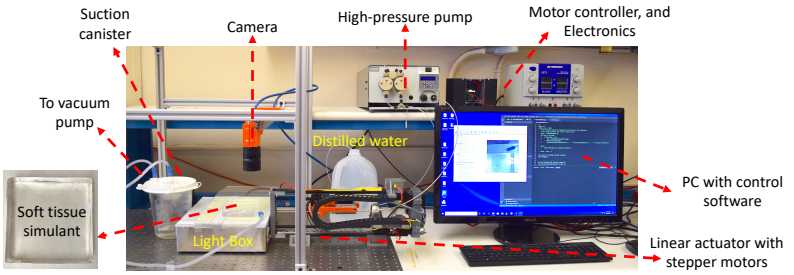

Fig. 5 Experimental setup to measure the depth of cut of waterjet in soft tissue. A linear actuator is used to drive the needle into the soft tissue. Once the needle is in the tissue, the pump is run with a given volumetric flow rate and after about 30 (s) the camera will take a photo to be processed with a MATLAB program to measure the DOC.

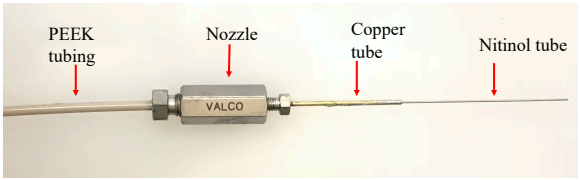

Fig. 6 Custom-designed water-jet needle with a copper tubing ($ID = 0.94$ mm, and $OD = 1.59$ mm) soldered to a superelastic material Nitinol (first needle: $ID = 0.32$ mm, and $OD = 0.58$ mm, and second needle: $ID = 0.24$ mm, and $OD = 0.33$ mm). The copper tubing is attached to a ferruled reducer, and then standard PEEK tubing.

$1\frac{mm}{s}$. This will ensure that the excess water will be sprayed back and will not be trapped in the channel to cause ballooning in the tissue. When the needle is inserted 1 cm into the tissue, the pump will be turned off and turned on again to ensure maximum depth of cut. After 30 seconds, and using the overhead high-resolution camera and the control software, a photo is taken and saved for further processing. For better visibility, edible food dye was added to the water. To study the effects of tissue stiffness, needle diameter, and flow rate on cut depth, 6 different tissue stiffnesses (10 %, 15 %, and 20 % G1650, and G1652 SEBS), 2 different needle diameters (first needle: $ID = 0.32$ mm, $OD = 0.58$ mm, and second needle: $ID = 0.24$ mm, $OD = 0.33$ mm), and different flow rates up to $100\frac{mL}{min}$ are tested. To make sure that the data are statistically significant, 5 experiments are done for each flow rate and the average of them is taken as the cut-depth. The photos are processed using a customized Matlab program that measures the depth of cut in front of the needle from the pixels of the photo based on the calibrated measurement provided by the ruler on the light-box.

2.4 Predictive Mechanics-based Model for Depth Of Cut (DOC)

In this part, the predictive mechanics-based model of depth of cut of waterjet in soft tissue is presented. This model is based on fracture mechanics and is dependent on waterjet, and tissue properties such as velocity, diameter, fracture toughness, and shear modulus.

The model developed for the penetration pressure is based on the fracture-mechanics-based force model presented in Barnett *et al.* [10], and the principles presented in [1]. The advantage of using methods based on fracture mechanics is that models based on this method have a better prediction especially when failure happens [10], and [1]. In waterjet cutting of soft tissue, when the velocity of waterjet is higher or equal with respect to the minimum velocity that can cause failure in soft tissue, the tissue will be cut and an initial crack will be formed. The crack is then widened to accommodate the waterjet column.

Fig. 7 depicts a simplified schematic of waterjet cutting soft tissue. First, a crack is initiated by waterjet, and then the crack opens to let the waterjet with diameter of D through. The waterjet displaces the tissue during penetration as demonstrated. Upon waterjet removal, the crack closes and reaches to the steady state diameter of d. Although several studies showed that waterjet cuts soft material with mode I crack propagation (similar to sharp needles) by wedging open the soft tissue [14], [53], and [54], others [51] showed that in needle-free injections, waterjet penetrates the cheek of human cadavers by formation of a cylinder-shaped holes. In Schramm-Baxter *et al.* [49], they divide the jet penetration into polyacryamide gels into three phases namely erosion, stagnation, and dispersion. They showed that during the erosion phase, the jet removed the gel and led to the formation of a cylindrical hole. Tagawa *et al.* [57] also observed a cylindrical hole in the penetration of microjects into the gelatin and artificial skin. To avoid complexity of the model and steer clear of finite element methods associated with sharp needle penetration models, the displacement of soft tissue with waterjet is considered to be cylindrical like [51].

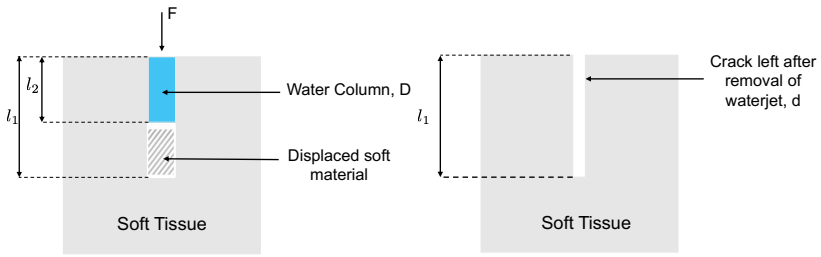

Fig. 7 Schematic of crack formed by the waterjet in soft tissue. (left) Waterjet initiates a crack and then the crack opens to accommodate the waterjet with diameter D followed by waterjet displacing the tissue, and (right) Crack left with diameter d after waterjet removal.

The fracture-based mechanics model that will be described in the following paragraphs is focused on predicting penetration pressure of waterjet P_w, and thus predicting depth of cut (DOC) defined by the following equations:

$$P_w = f(D, d, J_{IC}, \alpha, \mu) \tag{14}$$

and,

$$DOC = f(\rho, v, T, D, d, J_{IC}, \alpha, \mu) \tag{15}$$

In these equations, D, d, J_{IC}, α, μ, ρ, v, and T are waterjet diameter, steady-state diameter after waterjet removal, mode I fracture toughness, strain hardening factor, shear modulus, water density, waterjet velocity, and time, respectively.

As waterjet advances in the soft tissue, it does work on the soft tissue that equals to $F\delta l_2$, where F is the force exerted on soft tissue, and δl_2 is a differential insertion length. Then, waterjet forms a crack in the soft tissue and displaces the tissue to accommodate the diameter of the waterjet. The work done in advancing waterjet is equal to the sum of crack work δW_C, and strain energy stored in soft tissue while being displaced δE_S:

$$F\delta l_2 = \delta W_C + \delta E_S \tag{16}$$

The work associated with crack formation in the soft tissue δW_C can be expressed by the following equation:

$$\delta W_C = J_{IC}\delta A_C \tag{17}$$

In which $A_C = 2\pi(\frac{d}{2})l_1$ is the steady state area of the crack after waterjet removal. Thus, $\delta A_C = \pi d\delta l_1$ is the increment in crack area. Therefore equation (17) can be re-written as:

$$\delta W_C = J_{IC}\pi d\delta l_1 \tag{18}$$

In which J_{IC} is mode I fracture toughness ($\frac{J}{m^2}$) which is dependent on crack growth rate already developed in (13).

The strain energy stored in the soft solid can be defined by:

$$E_S = E_d + E_e \tag{19}$$

In which, E_d, and E_a are strain energy due to displacement of the soft tissue, and strain energy due to widening of the hole in the soft tissue while accommodating waterjet.

If we define $\delta E_d = \frac{\partial E_d}{\partial l_1}\delta l_1$, and $\delta E_e = \frac{\partial E_e}{\partial l_1}\delta l_1$, then $\delta E_S = \frac{\partial E_d}{\partial l_1}\delta l_1 + \frac{\partial E_e}{\partial l_1}\delta l_1 = (\frac{\partial E_d}{\partial l_1} + \frac{\partial E_e}{\partial l_1})\delta l_1$, and thus (16) can be re-written as:

$$F\delta l_2 = \left(J_{IC}\pi d + \frac{\partial E_d}{\partial l_1} + \frac{\partial E_e}{\partial l_1}\right)\delta l_1 \tag{20}$$

This equation relates the work done in advancing the waterjet to the fracture work and strain energy stored in the soft solid due to displacement and expansion.

According to conservation of volume, the volume of the displaced soft tissue to accommodate to the waterjet of diameter D is the same as the volume of the crack after waterjet removal:

$$\pi \left(\frac{D}{2}\right)^2 (l_1 - l_2) = \pi \left(\frac{d}{2}\right)^2 l_1 \tag{21}$$

Thus, $l_1 = \frac{D^2}{D^2-d^2} l_2 \rightarrow \frac{\delta l_1}{\delta l_2} = \frac{D^2}{D^2-d^2}$.

By dividing the sides of (20) by $A_w \delta l_2$, in which $A_w = \frac{\pi D^2}{4}$ is the cross sectional area of the waterjet, we can write:

$$P_w = \frac{F}{A_w} = \frac{4}{\pi D(1-(\frac{d}{D})^2)} \left[J_{IC} \pi \frac{d}{D} + \frac{1}{D} \left(\frac{\partial E_d}{\partial l_1} + \frac{\partial E_e}{\partial l_1} \right) \right] \tag{22}$$

This equation provides a prediction of the penetration pressure of waterjet into soft tissue. In order to have a closed form equation for it, one should find equations for $\frac{\partial E_d}{\partial l_1}$, and $\frac{\partial E_e}{\partial l_1}$.

In order to find the $\frac{\partial E_e}{\partial l_1}$, suppose that $d = 2r_1$, and $D = 2r_2$ in which r_1, and r_2 are radius of the crack in steady state, and radius of waterjet column, respectively. When waterjet penetrates into soft tissue, the ring of the crack expands from initial radius s_1 to final radius s_2. Suppose that these rings have thicknesses of ds_1, and ds_2 with unit heights. The concept of the expansion of the crack is depicted in Fig. 8.

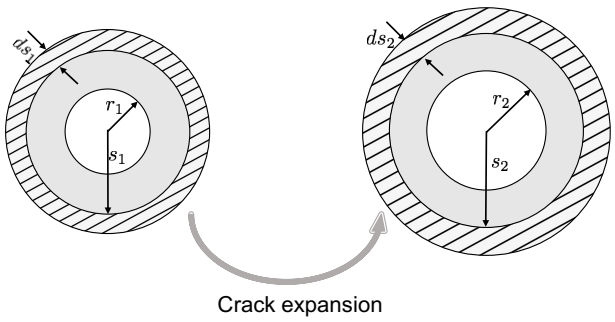

Fig. 8 Schematic of crack expansion from radius s_1 to s_2 in penetration of waterjet with radius r_2 into a crack with steady state radius of r_1.

Due to conservation of volume, the volume of the column is equal before and after the expansion:

$$\pi({s_1}^2 - {r_1}^2)(1) = \pi({s_2}^2 - {r_2}^2)(1) \tag{23}$$

Another result that is deducted from volume conservation is that the multiplication of the stretch ratios are one. Considering cylindrical coordinates (r, θ, z), one can write: $\lambda_r \lambda_\theta \lambda_z = 1$, in which λ_r, λ_θ, and λ_z are principal stretch ratios. With the assumption of plain strain expansion of the crack (i.e. expansion happens in plane), one can conclude that $\lambda_z = 1$. Since $\lambda_r = \frac{s_1}{s_2}$, it is easy to see that $\lambda_\theta = \frac{1}{\lambda_r} = \frac{s_2}{s_1}$.

In order to model the constitutive response of the soft tissue, Ogden model [40], and [41] is used in this paper. This model is proved to be a good fit for materials that go through strain hardening such as soft tissues [10]. The one-term Ogden model for an isotropic, incompressible, and hyperelastic material can be described as:

$$\phi = \frac{2\mu}{\alpha^2}({\lambda_1}^\alpha + {\lambda_2}^\alpha + {\lambda_3}^\alpha - 3) \tag{24}$$

Where ϕ, μ, α, and λ_i are strain energy density function ($\frac{J}{m^3}$), shear modulus, strain hardening, and the principal stretch ratios, respectively. Considering $\lambda_1 = \frac{s1}{s2}$, $\lambda_2 = 1/\lambda_1$, and $\lambda_3 = 1$, one can re-write the equation (24) as:

$$\phi = \frac{2\mu}{\alpha^2}\left[\left(\frac{s_1}{s_2}\right)^\alpha + \left(\frac{s_2}{s_1}\right)^\alpha - 2\right] \tag{25}$$

With above definition of strain energy density function, one can write:

$$\frac{\partial E_e}{\partial l_1} = \int_{r_1}^{\infty} \phi \, dV_1 = \int_{r_2}^{\infty} \phi \, dV_2 \tag{26}$$

In which, $dV_1 = 2\pi s_1 ds_1$, and $dV_2 = 2\pi s_2 ds_2$, are the volume change elements in crack expansion. Thus (26) can be written in the final form as:

$$\frac{\partial E_e}{\partial l_1} = \frac{\pi \mu D^2}{2\alpha^2} \int_1^{\infty} f\left(\frac{d}{D}, \gamma\right) d\gamma \tag{27}$$

In which, $f(\frac{d}{D}, \gamma)$ can be expressed in the closed form as:

$$f\left(\frac{d}{D}, \gamma\right) = \left(\frac{\gamma + \left(\frac{d}{D}\right)^2 - 1}{\gamma}\right)^{\frac{\alpha}{2}} + \left(\frac{\gamma}{\gamma + \left(\frac{d}{D}\right)^2 - 1}\right)^{-\frac{\alpha}{2}} - 2 \tag{28}$$

Considering $\alpha = 2$, this integral has an analytic solution but other than that it needs to be solved numerically. Appendix A provides a procedure for derivation of these equations.

Now that a closed form solution is found for $\frac{\partial E_e}{\partial l_1}$, it is time to find a similar formula for $\frac{\partial E_d}{\partial l_1}$. From volume conservation, we already know that $\lambda_r \lambda_\theta \lambda_z = 1$. If we take $\lambda_r = \lambda_\theta$, then we can write:

$$\lambda_r = \lambda_\theta = \frac{1}{\sqrt{\lambda_z}} = \frac{D}{d} \tag{29}$$

Then, the strain energy density function can be re-written as:

$$\phi = \frac{2\mu}{\alpha^2}(2{\lambda_r}^{\alpha} + {\lambda_r}^{-2\alpha} - 3) \tag{30}$$

Therefore:

$$\begin{aligned} \frac{\partial E_d}{\partial l_1} &= \pi \left(\frac{d}{2}\right)^2 (1)\phi = \\ \frac{\pi d^2}{d}\frac{2\mu}{\alpha^2}(2{\lambda_r}^{\alpha} + {\lambda_r}^{-2\alpha} - 3) &= \\ \frac{\pi D^2}{4}\frac{2\mu}{\alpha^2}[2\left(\frac{d}{D}\right)^{2-\alpha} + \left(\frac{d}{D}\right)^{2\alpha+2} - 3\left(\frac{d}{D}\right)^2] & \end{aligned} \tag{31}$$

Substituting (27), and (31) into (22), we can write the closed form mathematical solution for penetration pressure of waterjet in soft tissue as:

$$\begin{aligned} P_w = \frac{4}{D(1-(\frac{d}{D})^2)}\Bigg\{ J_{IC}\left(\frac{d}{D}\right) + \frac{D}{4}\frac{2\mu}{\alpha^2}\Bigg[\int_1^{\infty} f\left(\frac{d}{D},\gamma\right) d\gamma \; + \\ 2\left(\frac{d}{D}\right)^{2-\alpha} + \left(\frac{d}{D}\right)^{2\alpha+2} - 3\left(\frac{d}{D}\right)^2\Bigg]\Bigg\} \end{aligned} \tag{32}$$

Where, $f(\frac{d}{D},\gamma)$ is already given in (28). This equation provides a closed form solution for penetration pressure of the waterjet in soft tissue in terms of diameter of the waterjet, and crack as well as tissue mechanical properties. Crack dimensions should be such that the penetration pressure is minimized. It is assumed that the penetration occurs in this minimum penetration pressure.

Now that the penetration pressure can be predicted, we should develop a predictive model for depth of cut of waterjet in soft tissue. For this, the simple model shown in Fig. 9 is proposed, where v, D, and h are waterjet velocity ($\frac{m}{s}$), waterjet diameter (m), and cut-depth in soft tissue (m), respectively.

In order to find the depth of cut, the kinetic energy of the waterjet should be equated to the energy expended during waterjet penetration:

$$KE_w = E_C \tag{33}$$

Where KE_w is the kinetic energy of waterjet, and E_C is the consumed energy during waterjet penetration. KE_w can be calculated as follows:

$$KE_w = \int_0^T P\,dt = \int_0^T \frac{1}{2}\dot{m}v^2\,dt \tag{34}$$

In which P is the power of waterjet, and mass flow rate of water jet $\dot{m}$ can be defined as:

$$\dot{m} = \rho A_w v = \rho\frac{\pi D^2}{4}v \tag{35}$$

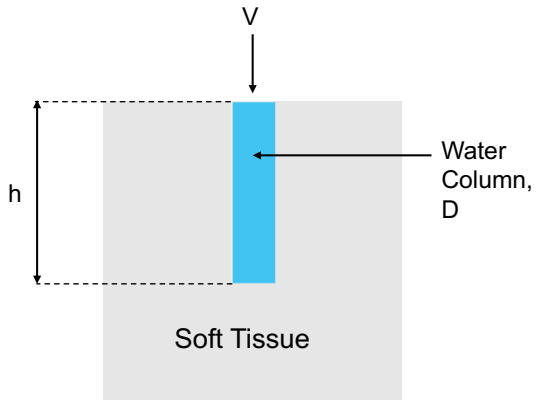

Fig. 9 Schematic of the simple model for depth of cut of waterjet in soft tissue. v, h, and D are velocity of waterjet ($\frac{m}{s}$), cut-depth (m), and waterjet diameter (m).

Thus, 34 can be re-written as:

$$KE_w = \int_0^T \frac{1}{2}\rho \frac{\pi D^2}{4} v^3 \, dt \tag{36}$$

For the consumed energy during waterjet penetration, we can write:

$$E_C = P_w \frac{\pi D^2}{4} h \tag{37}$$

Now, equating (36), and (37), one can write:

$$h = \frac{\frac{1}{2}\rho \int_0^T v^3 \, dt}{P_w} \tag{38}$$

Where, P_w can be calculated using (32). This equation gives a closed form physics-based mathematical solution for depth of cut of waterjet in soft tissue as a function of waterjet properties (diameter, and velocity) as well as soft tissue mechanical characteristics (constitutive response, and fracture toughness).

Equation (38) will overpredict the depth of cut of waterjet in soft tissue since it does not consider the fact that a large proportion of the jet's kinetic energy is dissipated during penetration into soft solid. In order to have a more accurate description for DOC, we also need to take the effects of these parameters into consideration. Next section is going to deal with this and provide a more accurate model to predict the depth of cut of waterjet in soft tissue.

The volume of water coming out of the nozzle can be calculated by the following equation:

$$V = A_w \int_0^T v dt = \pi \frac{D^2}{4} vT \tag{39}$$

In which, A_w, T, v, and D are cross sectional area of waterjet (m^2), time (s), waterjet velocity ($\frac{m}{s}$), and waterjet diameter (m), respectively.

2.4.1 Lumped Parameters Fluid Model

The detailed shape of the surface of cut deeply influences the efficiency of the cutting process. In particular, the geometry of the excavated channel determines the amount of injected energy that actually reaches the soft tissue walls, and the fraction that is lost in the backflow. While the full process could be accurately simulated via finite-element methods or through smooth particle hydrodynamics codes, we develop a simple lumped parameters model, able to retrieve a realistic value for the depth of cut in different tissues, with minimal computational cost. The model has a free parameter, that can be fitted to retrieve best results for a given combination of tissue and needle size.

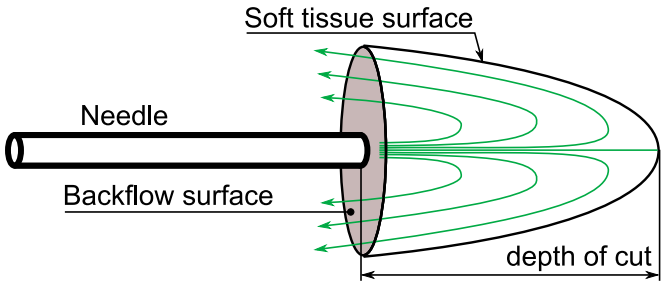

Fig. 10 Simplified view of the flow field inside the region of cut: injected water impacts the surface of cut in the stagnation point and backflows from the sides.

We assume that the fluid behavior can be well approximated by the scheme in figure 10. Part of the injected energy flux Φ_E^{inj} acts on the soft tissue walls of area A_{surf}, partly backflows from the surface with area A_{out}, and partly may be dissipated by viscous forces. Of the three, only the first one produces useful cutting work, such that (38) should be detailed further. As the energy is spread from the injection area $A_{\text{inj}} = \pi(D/2)^2$ equal to the needle internal cross section, towards the side and backflow surfaces, the energy flux is to be scaled by a factor $A_{\text{inj}}/(A_{\text{surf}} + A_{\text{out}})$. Of this energy, only the fraction $A_{\text{surf}}/(A_{\text{surf}} + A_{\text{out}})$ reaches the walls, the rest being lost in the backflow. Equation 38 becomes:

$$h = \frac{1}{P_w} \int_0^T \left(\frac{\Phi_E^{inj} - P_{visc}}{A_{\text{inj}}} \right) \left(\frac{A_{\text{inj}}}{A_{\text{surf}} + A_{\text{out}}} \right) \left(\frac{A_{\text{surf}}}{A_{\text{surf}} + A_{\text{out}}} \right) \mathrm{d}t \tag{40}$$

where P_{visc} accounts for the energy dissipated by viscous forces. These terms injected energy, the soft tissue cutting surface and backflow areas assuming a given shape for the surface of cut, and the power of viscous forces will be detailed in the next paragraphs.

Injected energy The amount of energy injected per unit time by the needle, previously expressed as $\frac{1}{2}\rho v^3 A_{\text{inj}}$, can be improved from an analysis of the flow inside the needle. The velocity in the needle channel can be assumed to follow a Poiseuille profile [25], changing from a maximum value at the channel centerline to zero velocity at the needle walls:

$$v(r) = \frac{2Q}{\pi}\frac{R^2 - {r_p}^2}{R^4} \tag{41}$$

with Q the volumetric flow rate in $[\text{m}^3/\text{s}]$, $R = D/2$ the needle inlet radius and r_p the considered radial position. The injected energy flux thus reads:

$$\Phi_E^{\text{inj}} = \int_{A_{\text{inj}}} \frac{\rho v^2}{2}\mathbf{v}\cdot \mathrm{d}\mathbf{S} \equiv \int_{A_{\text{inj}}} \frac{\rho v^3}{2}\,\mathrm{d}S = \frac{\rho Q^3}{\pi^2 R^4} \quad \left[\frac{\text{J}}{\text{s}}\right] \tag{42}$$

The term $\frac{1}{2}\rho v^3$ appearing in Eq. (38) thus transforms into (except for the viscous dissipation term, treated later on):

$$\frac{\rho v^3}{2} \;\rightarrow\; \frac{\Phi_E^{\text{inj}}}{A_{\text{inj}}} \quad \left[\frac{\text{J}}{\text{m}^2\,\text{s}}\right] \tag{43}$$

Surface of cut model As an approximation, we assume the shape of the surface of cut can be well described by an ellipsoid (see Fig. 11), with one axis equal to the depth of cut h, and the other two axis equal to $b = \eta h$ with eccentricity η. As the depth of cut grows in time during the water-cut process, the ellipsoid is supposed to expand keeping the same value for the eccentricity. This area growth progressively reduces the energy deposited per unit surface, and thus reduces the effect of the waterjet, explaining experimental data.

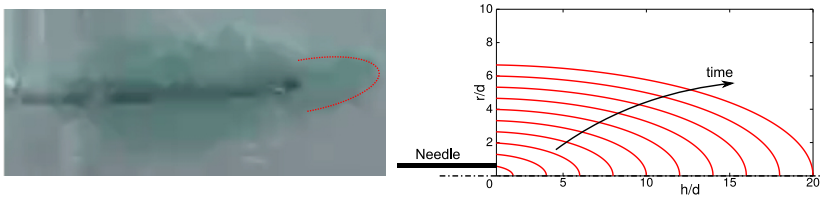

Fig. 11 Approximation of the surface of cut via ellipsoid. Left: superposition with experiment. Right: growth in time with constant aspect ratio.

As two semi-axes of the ellipsoid are the same, the surface area is that of half of either an oblate ($\eta > 1$) or prolate ($\eta < 1$) spheroid, reading:

$$A_{\text{surf}} = \begin{cases} \pi b^2 \left[1 + \frac{h^2}{eb^2} \tanh^{-1}(e)\right] \ , \ e^2 = 1 - \frac{h^2}{b^2} & \text{if} \quad \eta > 1 \\ \pi b^2 \left[1 + \frac{h}{eb} \sin^{-1}(e)\right] \ , \ e^2 = 1 - \frac{b^2}{h^2} & \text{if} \quad \eta < 1 \\ 2\pi h^2 & \text{if} \quad \eta = 1 \end{cases} \tag{44}$$

And from the semi-axis b and the outer needle diameter d_{out}, the backflow area is found as:

$$A_{\text{out}} = \pi \left[b^2 - (d_{out}/2)^2\right] \tag{45}$$

In general, the shape of the cutting surface can depend on the tissue stiffness properties. Despite the crude simplicity of the fluid model developed here, taking η as a free parameter fitted on experimental data, will allow to reproduce closely the measured DOC. The procedure will be detailed in Section 3.3.1, and η will be treated as a free parameter for the time being.

Viscous dissipation of energy Viscous forces can dissipate part of the injected energy into heat. However, preliminary analysis suggests that their effect is rather small, amounting to roughly the 2.5% of the injected energy, depending on the operating conditions. For this reason, we model viscous losses using a simple lumped-parameters model.

We assume most of the energy is dissipated on a cylindrical surface, where water backflows. This is equivalent to considering the power lost by friction for a water column moving inside a fixed medium. The scheme is shown in Fig. 12.

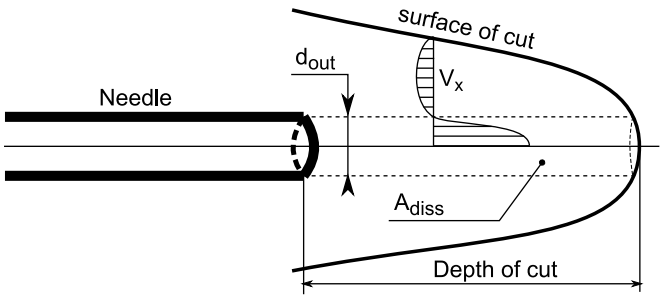

Fig. 12 Effective area where the bulk of viscous dissipation happens.

The power dissipated by viscous forces P_d can be written as:

$$P_d = \tau A_d \langle U \rangle \tag{46}$$

where τ is the viscous stress tensor; A_d the area along which the velocity reverses and most of the dissipation is thus supposed to take place; $\langle U \rangle$ the

average flow velocity across the considered section. We take the value of $\langle U \rangle$ equal to half of the average inlet fluid velocity U, accounting for the fact that most dissipation likely happens close to the nozzle exit, and decreases moving towards the stagnation point. The dissipation area is assumed to be defined by the outer needle diameter, and a length equal to the depth of cut: $A_d = \pi d_{out} h$. The viscous stress term τ is evaluated by estimating the radial derivative using the $\langle U \rangle$ velocity:

$$\tau = \mu \frac{\mathrm{d} \langle U \rangle}{\mathrm{d}r} = \mu \frac{U/2}{d_{out}/2} = \mu \frac{U}{d_{out}} \tag{47}$$

with μ the dynamic viscosity of water, which in standard conditions reads: $\mu \approx 8.9 \times 10^{-4}$[Pa s]. Therefore, the dissipated power reads:

$$P_d = \tau A_d \langle U \rangle = \left(\mu \frac{U}{d_{out}} \right) (\pi d_{out} h) \frac{U}{2} = \frac{\pi}{2} \mu U^2 h \tag{48}$$

The small value assumed by this term justifies *a posteriori* its simplified treatment. For the same reason, while this term should appear in (40), it will be directly neglected.

Numerical integration The value of the depth of cut appearing in (40) can be readily integrated numerically. By introducing the value for Φ_E^{inj} derived in (42) and differentiating both sides with respect to time, we obtain:

$$\frac{\mathrm{d}h}{\mathrm{d}t} = \frac{1}{P_w} \frac{\rho Q^3}{\pi^3 R^6} \frac{A_{\mathrm{inj}} A_{\mathrm{surf}}}{(A_{\mathrm{surf}} + A_{\mathrm{out}})^2} \tag{49}$$

where the viscous power dissipation was neglected as discussed in previous paragraph. This is an ordinary differential equation, where A_{surf} and A_{out} are function of h, and can be readily integrated using standard methods such as Runge-Kutta integrators.

We shall finally note that the model described here can be used for a dual purpose:

- It can allow to reproduce efficiently and accurately the evolution of depth of cut in time, once a proper calibration of η is assigned for a certain tissue and needle size, or
- It can be employed by assigning a given value of η (for example $\eta = 1/3$ or following optical measurements of the surface of cut at different times), and used to estimate the mechanical properties of the material, which better reconstruct the measured depth of cut.

In any case, once η is known or assigned, the simplicity of the model allows for real-time prediction of the depth of cut with minimal computational efforts.

3 Results

In this section, the proposed model is validated with experimental data. In order to do so, the results of characterization of the SEBS soft tissue simulants using static compression tests, SHPB tests, and fracture toughness tests are presented.

3.1 Mechanical Properties of SEBS Soft Tissue Simulants (constitutive response, and fracture toughness)

Fig. 13 shows an example of the results of the static compressive stress vs. stretch ratio response of SEBS soft tissue simulants at uniaxial nominal strain rates of 0.001, 0.01, and 0.1 s^{-1}. Ogden strain energy density function is calibrated to represent the constitutive response of each soft tissue simulant at the specified strain rate. The results of the static compressive strain vs. stretch ratio of the SEBS soft tissue simulants showed that the constitutive response is not sensitive to low rates of strain, and that Ogden model can describe the behavior of these soft tissue simulants with a reasonable agreement.

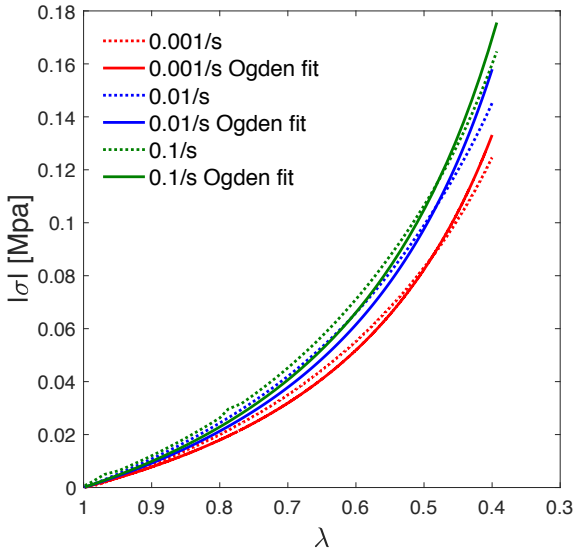

Fig. 13 Example static compression test results (stress vs. stretch ratio) on 20% SEBS G1650 soft tissue simulants with the corresponding Ogden fit. Tissue properties are measured at three strain rates of $0.001s^{-1}$, $0.01s^{-1}$, and $0.1s^{-1}$. The same J-shaped stress vs. stretch ratio with the same trend is also observed for other tissue simulants. For each strain rate, two tests are conducted and the averages of these tests are shown in this figure.

Fig. 14 shows example results of the high strain rate compressive stress vs. stretch ratio response of SEBS soft tissue simulants. From this figure, one can see that the SEBS soft tissue simulants go through strain hardening at high strains, and that the response is strain rate dependent. In order to capture the shape of the strain hardening response, uniaxial compressive strains in excess of 0.3 are required (note that the figures show compressive stress vs. stretch ratio responses; however for compressive tests relation $\lambda = 1 - \varepsilon$ holds between strain (ε) and stretch ratio (λ)). Comparing these results to results

of low strain rate (0.001 to 0.1 s^{-1}) static compression tests on SEBS reveal that the response of these soft tissue simulants is sensitive to increasing rates of strain as shown for real biological tissues [55]. The strain rate sensitivity of the soft tissue simulants is described by increasing shear modulus with strain rate. This shows that strain rate sensitivity is related to the viscous properties of the soft tissue simulants.

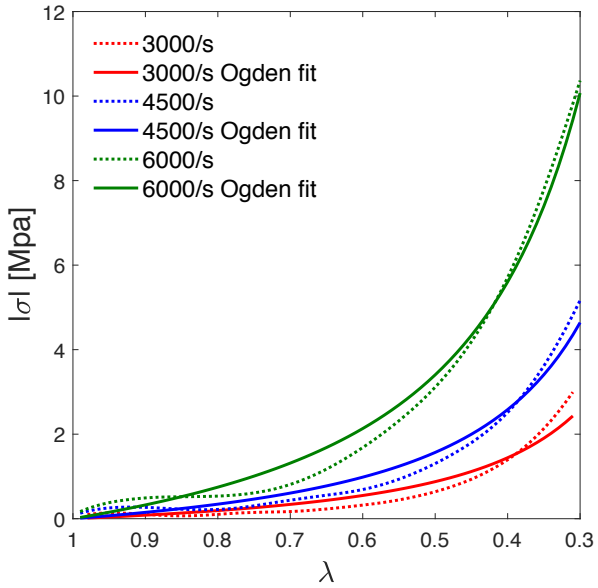

Fig. 14 Example SHPB compression test results on 15% SEBS G1650 soft tissue simulants. Tissue properties are measured at three strain rates of $3000s^{-1}$, $4500s^{-1}$, and $6000s^{-1}$. The same J-shaped stress vs. stretch ratio with the same trend is also observed for other tissue simulants. For each strain rate, three tests are conducted and the averages of three tests are shown in these figures.

Table 2, and 3 represents the Constants of one-term Ogden strain energy density function, that are shear modulus, and strain hardening factor of the soft solid that characterize the constitutive response of the G1650, and G1652 SEBS soft tissue simulants. The strain rate sensitivity of the constitutive response is described by an increase in shear modulus with increasing strain rate, while strain hardening factor is kept constant. α is calculated by fitting the Ogden model to experimental data at 0.001 s^{-1}, and this α is used as the strain hardening factor for the rest of strain rates. Thus the optimization problem only had one constant to calculate, which is the shear modulus.

Fig. 15 depicts the shear modulus vs. strain rate data with a linear fit. As it is evident from this figure, the shear modulus is a linear function of the strain rate at high rates of strain. Thus it is proposed that shear modulus can be

Table 2 Mechanical properties of G1650 SEBS tissue simulants obtained from Ogden fit to data. μ (kPa), α, and R^2 are shear modulus, strain hardening factor, and goodness of the Ogden fit, respectively.

G1650 10%				G1650 15%				G1650 20%			
$\dot{\varepsilon}(s^{-1})$	$\mu(kPa)$	α	R^2	$\dot{\varepsilon}(s^{-1})$	$\mu(kPa)$	α	R^2	$\dot{\varepsilon}(s^{-1})$	$\mu(kPa)$	α	R^2
0.001	7.01	1.25	0.99	0.001	16.65	1.7	1	0.001	22.68	1.08	0.99
0.01	7.28	1.25	0.99	0.01	16.75	1.7	0.99	0.01	26.89	1.08	0.99
0.1	8.82	1.25	0.99	0.1	19.54	1.7	0.99	0.1	28.88	1.08	0.99
3000	193.85	1.25	0.92	3000	249.25	1.7	0.93	3000	278.03	1.08	0.93
4500	511.40	1.25	0.96	4500	554.58	1.7	0.97	4500	605.60	1.08	0.97
6000	761.50	1.25	0.97	6000	967.93	1.7	0.98	6000	993.87	1.08	0.98

Table 3 Mechanical properties of G1652 SEBS tissue simulants obtained from Ogden fit to data. μ (kPa), α, and R^2 are shear modulus, strain hardening factor, and goodness of the Ogden fit, respectively.

G1652 10%				G1652 15%				G1652 20%			
$\dot{\varepsilon}(s^{-1})$	$\mu(kPa)$	α	R^2	$\dot{\varepsilon}(s^{-1})$	$\mu(kPa)$	α	R^2	$\dot{\varepsilon}(s^{-1})$	$\mu(kPa)$	α	R^2
0.001	2.77	1.26	0.99	0.001	7.34	1.41	1	0.001	11.60	1.16	0.99
0.01	2.92	1.26	0.99	0.01	8.12	1.41	0.99	0.01	15.96	1.16	0.99
0.1	4.18	1.26	1	0.1	13.76	1.41	0.99	0.1	22.76	1.16	0.99
3000	229.93	1.26	0.94	3000	307.83	1.41	0.93	3000	334.69	1.16	0.95
4500	429.22	1.26	0.96	4500	537.95	1.41	0.97	4500	559.89	1.16	0.97
6000	808.46	1.26	0.98	6000	952.07	1.41	0.98	6000	961.11	1.16	0.98

Table 4 Linear fit to shear modulus vs. strain rate data. Shear modulus can be extrapolated to higher strain rates based on these fits according to the intended application. μ (MPa), $\dot{\varepsilon}(s^{-1})$, and R^2 are shear modulus, strain rate, and goodness of the linear fit, respectively.

tissue type	linear fit	R^2
G1650 10%	$\mu = 1.89 \times 10^{-4}\dot{\varepsilon} - 0.36$	0.99
G1650 15%	$\mu = 2.4 \times 10^{-4}\dot{\varepsilon} - 0.49$	0.99
G1650 20%	$\mu = 2.39 \times 10^{-4}\dot{\varepsilon} - 0.45$	1
G1652 10%	$\mu = 1.93 \times 10^{-4}\dot{\varepsilon} - 0.38$	0.97
G1652 15%	$\mu = 2.15 \times 10^{-4}\dot{\varepsilon} - 0.37$	0.97
G1652 20%	$\mu = 2.09 \times 10^{-4}\dot{\varepsilon} - 0.32$	0.97

extrapolated to higher rates of strain based on the intended application (please see Table 4). For example, for waterjet fracture-directed steerable needles [7], the shear modulus of the soft tissue at strain rates in the order of 10^4 is required. Thus, extrapolating data to higher strain rates will give us the strain rate required for these applications.

Comparison of the results of static compressive tests and SHPB tests reveal that the constitutive response of SEBS soft tissue simulants are sensitive to high rates of strain and does not change much at low strain rates.

Table 5, and 6 represent the results of fracture toughness tests on SEBS soft tissue simulants. At least two tests are done for each test rate and the average of the results are provided here.

Measuring the fracture toughness data in crack growth rates associated with waterjet penetration is found to be the out of scope of this research. Therefore in order to have an approximation of the fracture toughness data at higher crack growth rates, data at low rates are extrapolated to higher crack

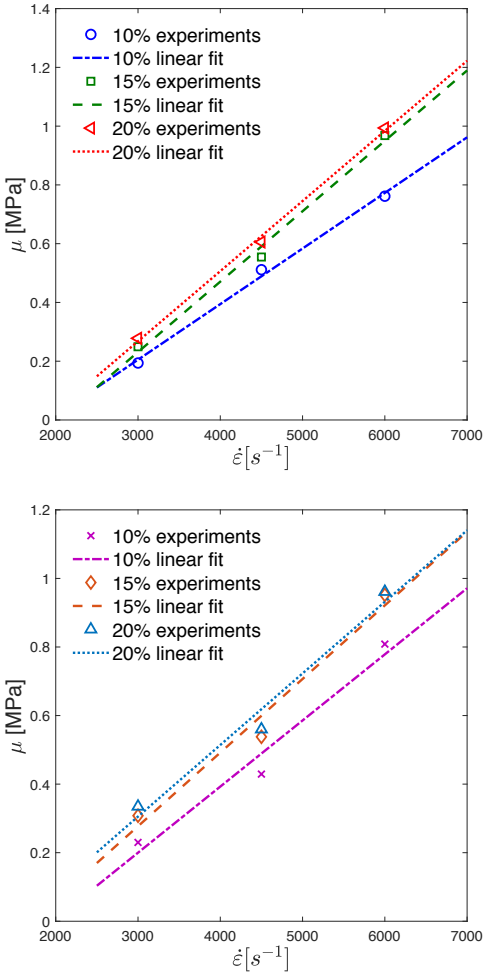

Fig. 15 Shear modulus vs. strain rate and linear fit to data to extrapolate to higher strain rates. (up) G1650 SEBS soft tissue simulants, and (down) G1652 SEBS soft tissue simulants. Due to the linear pattern in high strain rates, the shear modulus can be extrapolated to the desired strain rate depending on the application.

Table 5 Fracture toughness (J_{IC}) of G1650 SEBS soft tissue simulants at three test rates of 0.1, 0.5, and 1 $\frac{mm}{s}$. Crack growth rate ($\dot{r}$) is assumed to be half of the rate at which the test is performed.

G1650 15%			G1650 20%		
Test Velocity ($\frac{mm}{s}$)	$\dot{r}$ ($\frac{mm}{s}$)	J_{IC} ($\frac{J}{m^2}$)	Test Velocity ($\frac{mm}{s}$)	$\dot{r}$ ($\frac{mm}{s}$)	J_{IC} ($\frac{J}{m^2}$)
0.1	0.05	7.44	0.1	0.05	26.14
0.5	0.25	10.81	0.5	0.25	26.55
1	0.5	14.43	1	0.5	49.51

Table 6 Fracture toughness (J_{IC}) of G1652 SEBS soft tissue simulants at three test rates of 0.1, 0.5, and 1 $\frac{mm}{s}$. Crack growth rate ($\dot{r}$) is assumed to be half of the rate at which the test is performed.

G1652 15%			G1652 20%		
Test Velocity ($\frac{mm}{s}$)	$\dot{r}$ ($\frac{mm}{s}$)	J_{IC} ($\frac{J}{m^2}$)	Test Velocity ($\frac{mm}{s}$)	$\dot{r}$ ($\frac{mm}{s}$)	J_{IC} ($\frac{J}{m^2}$)
0.1	0.05	4.43	0.1	0.05	8.62
0.5	0.25	7.61	0.5	0.25	11.85
1	0.5	9.24	1	0.5	18.01

growth rates to approximate the fracture toughness of the SEBS soft tissue simulants at high crack growth rates.

3.2 Experimental Results: DOC of Waterjet in Soft Tissue is a Function of Waterjet as well as Soft Tissue Properties

Fig. 16 shows the average measurements of depth of cut as a function of fluid velocity with different percentages of SEBS tissues, and needles with inner diameters of 0.24 mm, and 0.32 mm. Fig. 17, and Fig. 18 show the depth of cut of water-jet as a function of needle diameter, and tissue stiffness, respectively.

From these experimental data, one can derive the following conclusions:

- Depth of cut is almost a linear function of flow rate (Q) when the width of the water-jet nozzle is sufficiently small.
- The depth of cut is a function of waterjet velocity v (and thus volumetric flow rate Q), stiffness of the tissue, and diameter of the needle (D). It has a direct relationship with flow rate, and inverse relationship with tissue stiffness and needle diameter.
- There is a minimum flow rate that the fracture in the tissue actually begins, and this flow rate is dependent on the stiffness of the tissue. As the tissue becomes stiffer, larger flow rate is required to cause fracture in the tissue.
- For smaller diameter needle, the minimum flow rate needed to cut is lower. This is likely due to the higher contact stress which leads to the earlier fracture of the tissue. The higher residual jet velocity associated with smaller needle diameter after the initial penetration also leads to larger DOC.
- For higher flow rates, water cuts more of the surrounding tissue, which is undesirable. For fracture-directed steerable needles [8], larger depth of cut is not necessary and it is important that a small amount is cut and then the needle follows the path.
- Observation that the depth of cut of a smaller diameter needle is larger explains the reason of tissue fracture by water-jet. According to the equation 12, as the diameter of the needle decreases the velocity of water-jet increases and thus the kinetic energy of water-jet increases. The increased kinetic energy is the reason that the depth of cut of water-jet needle with smaller diameter is larger than that of with bigger diameter.

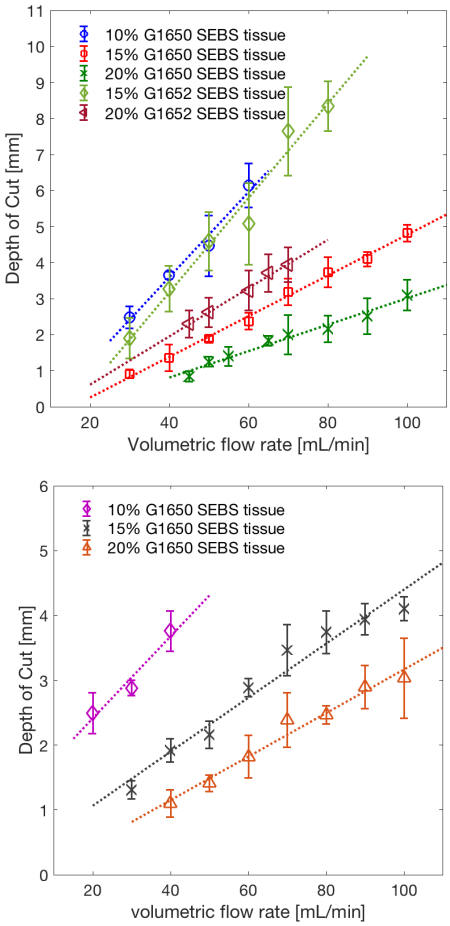

Fig. 16 Experimental DOC of waterjet in SEBS soft tissue simulants vs. volumetric flow rate. (up) DOC vs. Flow Rate for the Needle with 0.32 mm inner diameter (ID) in SEBS Tissue Simulants, and (down) DOC vs. Flow Rate for the Needle with 0.24 mm ID in SEBS Tissue Simulants. The data show the average of 5 tests for each volumetric flow rate, and error bars show the standard deviation of the data.

3.3 Validation of the Predictive Model with Experimental Results, and Tissue Properties

In order to validate the proposed model for DOC of waterjet in soft tissue, experimental DOC, and tissue properties are obtained in the previous sections. It is assumed that the penetration occurs at the minimum of the P_w vs. $\frac{d}{D}$ given in (32). *fmincon* function in MATLAB is used to solve this optimization

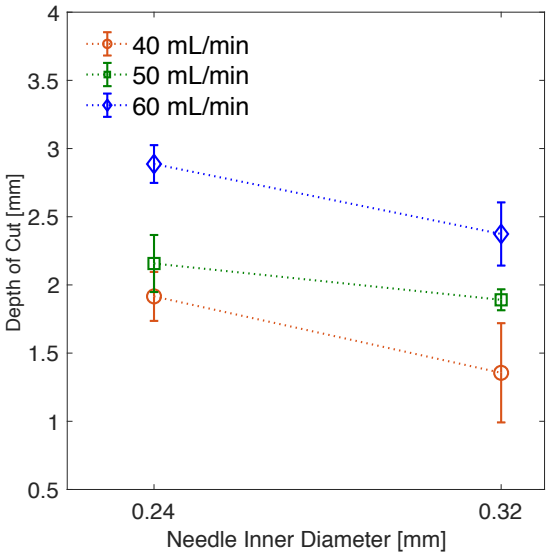

Fig. 17 DOC of waterjet as a Function of Needle Diameter for two needle inner diameters tested in this study ($D = 0.32mm$, and $D = 0.24mm$). The volumetric flow rate and tissue stiffness are held constants. The result is shown as an example for 15% G1650 SEBS soft tissue simulants. The data are the average of 5 experiments and the error bars are standard deviation of the data.

Table 7 Calculated values of P_w from (32) at different waterjet velocities for 15%, and 20% G1652 SEBS soft tissue simulants for the needle with $D = 0.32mm$.

G1652 15%, $D = 0.32mm$		G1652 20%, $D = 0.32mm$	
$v(\frac{m}{s})$	$P_w(MPa)$	$v(\frac{m}{s})$	$P_w(MPa)$
6.22	5.41	9.33	6.89
8.29	7.55	10.37	7.73
10.36	9.68	12.44	9.42
12.44	11.81	13.47	10.27
14.51	13.94	14.51	11.11
16.59	16.08		

problem and find a $\frac{d}{D}$ that minimizes P_w given in (32) based on the given tissue properties. The calculated values for P_w for G1652 SEBS soft tissues at different waterjet velocities used in the validation of the model are given in Table 7. The values for other tissues can be calculated in a similar fashion and are not included for brevity.

In Figure 19 we compare the outcome of the model to the experimental values of the depth of cut vs time for the tissue obtained from the G1652-15% and 20%, with the 0.32 mm inner diameter needle and with flow velocities of 10.37 and 14.51 $\frac{m}{s}$, respectively. The value of η has been chosen *ad hoc* to match the experimental results, equal to the value of 0.75 for the first and 1.8

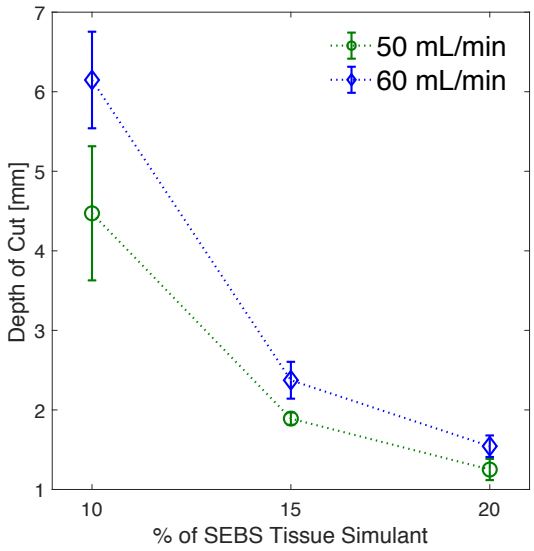

Fig. 18 DOC as a Function of percentage of G1650 SEBS soft tissue simulants. The volumetric flow rate and inner diameter of the needle (D = 0.32 mm) are held constants. The data shown are the average of 5 experiments, and the error bars are the standard deviation of the data.

for the latter. A more detailed discussion on the choice of the ellipsoid aspect ratio η is provided in Section 3.3.1.

The Integration is performed with a starting condition of $h = 0$. To help the first integration steps, we assume that for values of $h < d_{out}/2$, at the very beginning of the cutting process, the surface of cut is not an ellipsoid, but a simple cone with d_{out} as base. This has no visible impact on the solution, but avoids the initial singularity in the ellipsoid for $h = 0$, which may crash the integration.

3.3.1 Ellipsoid aspect ratio

We are interested here to prove the flexibility of the fluid model and check how accurately we are able to reproduce experimental values for the DOC by fitting the value of the free parameter η. As mentioned previously, writing the aspect ratio η of the ellipsoid as a function of the penetration pressure gives us the freedom necessary to fit closely to the experimental data.

Considering the results reported in Table 7, we run the fluid model for every velocity-P_w condition, finding the value of η which reproduces best DOC value at 30 seconds. This value is shown in Figure 20-Up, for different tissues and needles. A parabolic least-squares fit shows to reproduce fairly well the relation $\eta - P_w$. The values of the coefficients are reported in Table 8, following the

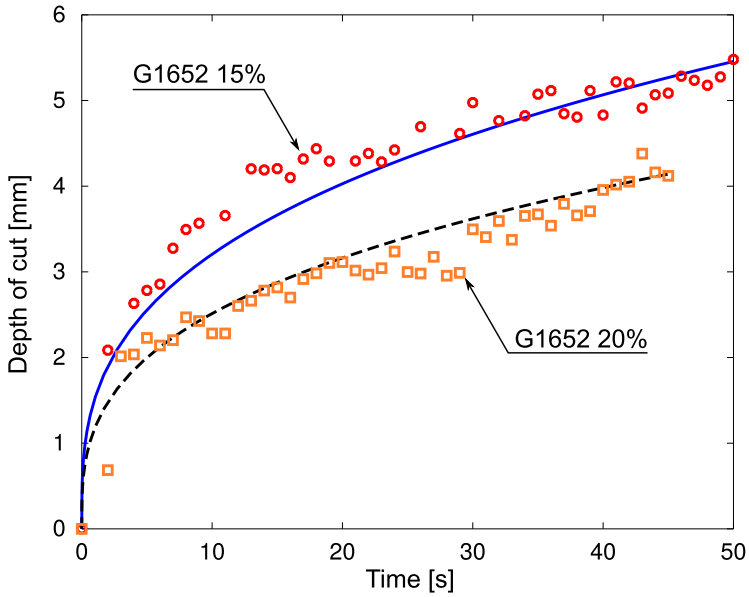

Fig. 19 DOC vs. time for 15% and 20% G1652 tissues; Experimental results (symbols) vs fluid model (lines) with best-fitting η. Needle diameter $D = 0.32mm$, and waterjet velocities (for G1652 15% $v = 10.36\frac{m}{s}$, and for G1652 20% $v = 14.51\frac{m}{s}$) are remained constant.

Table 8 Coefficients from parabolic least-squares fitting of η as a function of P_w (equation 50), for different tissues and needles; N1: $D = 0.32$ mm, N2: $D = 0.24$ mm.

	G1650 15% N1	G1650 20% N1	G1652 15% N1	G1652 20% N1	G1650 15% N2	G1650 20% N2
a	5.11e-15	8.22e-14	1.81e-14	1.65e-14	6.49e-16	7.12e-15
b	-3.31e-07	-2.52e-06	-5.21e-07	-4.86e-07	-8.90e-08	-5.44e-07
c	6.53e+00	2.27e+01	4.18e+00	4.91e+00	4.54e+00	1.39e+01

relation (with P_w in Pascal):

$$\eta = aP_w^2 + bP_w + c \tag{50}$$

The fitted expression for $\eta(P_w)$ was then inserted into the model, to reproduce the value of the DOC at 30 seconds. A good agreement is shown in Figure 20. While a physically sound procedure would be desirable for future modeling, the present results fully confirm the flexibility of the present model, which is able to retrieve the DOC to a good approximation, once η is tuned on the proper tissue-needle configuration.

4 Discussion

In this paper, a mechanics-based model is proposed for DOC of waterjet in soft tissue that only needs the properties of the tissue and the waterjet to

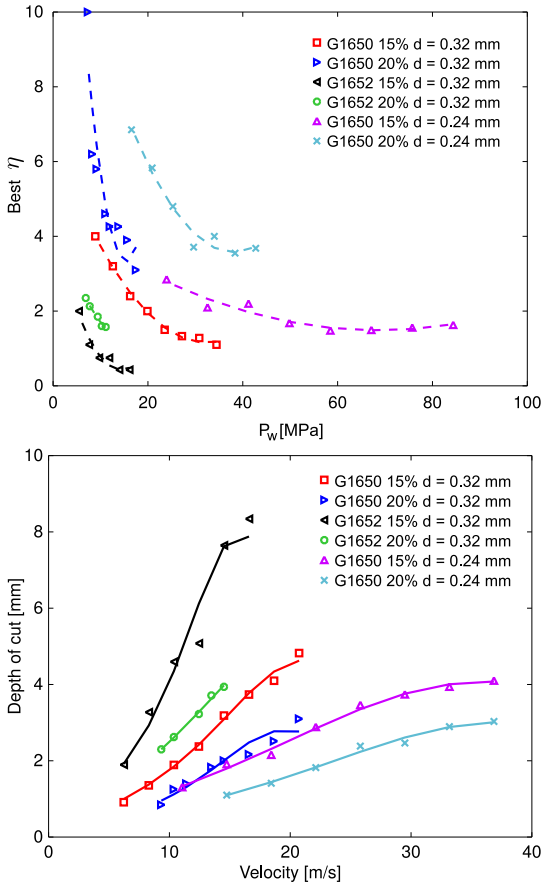

Fig. 20 Up: values of η that match the DOC at 30 seconds (symbols), and parabolic fit (dashed lines). Down: DOC prediction from the fitted η (solid lines) and experimental values (symbols).

predict the DOC. Unlike other models discussed in the introduction section that their parameters are tuned based on the experiments, the proposed model is independent of the experiments and is only dependent on the mechanical properties of the tissue being cut, and the operating properties of the waterjet.

The model developed for penetration pressure in this paper is based on the fracture mechanics-based force model developed in [10], and [29]. The process of crack formation in the soft solid show that both fracture toughness and constitutive response are important parameters in determining the penetration pressure. The solid goes through deformation before cracking starts. The advantage of using methods based on fracture mechanics is that models based

on this method can predict better especially when failure happens [10], and [1]. This is specifically important for waterjet cutting soft tissue since the tissue goes through failure when fracture happens. Traditionally, researchers utilized fracture mechanics-based models for cutting of industrial materials [5], [27], and [43]. This method has recently been used to model the needle penetration into soft materials [6], and [29]. By equating the work done in advancing waterjet to the sum of the energy for tissue fracture and stored strain energy in soft tissue, the penetration pressure of waterjet is modeled in this paper. The developed penetration pressure model is a function of tissue mechanical characteristics such as fracture toughness, and shear modulus as well as waterjet properties such as diameter. Since soft tissue is viscoelastic, its properties such as shear modulus and fracture toughness are strain rate dependent. Therefore, in order to have a better validation of the model, these properties should be measured in strain rates corresponding to waterjet cutting of soft tissue.

The work done in this paper characterized the response of the soft material while going through failure with waterjet, and provided a mechanics-based model to predict the DOC of waterjet in soft material. This work will be the foundation for research in waterjet-assisted surgery, and waterjet steerable needles. The penetration mechanism of the waterjet in soft tissue can be determined by failure mechanics of the soft tissue being penetrated. Criteria that can be used for soft tissue failure include: comparison of the local stress induced by waterjet impact to a critical stress, and comparison of the energy density input to the tissue to a critical energy density or work of fracture. The latter is the used method in this paper.

There are many advantages that are reported in literature for use of waterjet in medical applications. For instance it is proved that when using high-pressure waterjet for surgical wound debridement for abrasion of necrotic tissue, the treatment is performed in one session [9], [12] lowered the risk of infection [21], and less cost in comparison to the usual surgical debridement [28]. Other advantages are less intraoperative hemorrhage [9], and no thermal damage [9] in comparison to the common approaches. Because of the mentioned advantages, and promising results with waterjet, it was worth that the efficacy of the operations performed by waterjet was increased by providing closed-form mathematical equations to predict the DOC of waterjet as we did in this paper.

From, the DOC vs. time response of the waterjet cutting soft tissue presented in Fig. 19, one can see that the depth of cut of waterjet increases with higher slope at the beginning of cutting, and this slope decreases by increasing time that imply the dependence of the energy of waterjet on depth of penetration. This result is consistent with other studies such as [9] where the authors mentioned that the highest impact of the waterjet can be achieved at the very beginning when the waterjet hits soft tissue, and after that the water starts to flow radially that results in decrease of the impact of the jet. This result is also consistent with the result of the DOC vs. time presented by Morad *et al.* [34] in which the slope of the DOC vs. time decreased after about 30 (s), and also with the results of depth of cut vs. time presented in [35], [52], and

[57]. In other words, the effective velocity of the waterjet in soft medium is less than the velocity of waterjet coming out of the nozzle. This result is consistent with the result presented in [36] that the effective velocity of the projectile in the viscoelastic medium is lower than the velocity measured before the impact happens.

Several studies also confirm our results that the depth of waterjet penetration depends on the material properties of the penetrated soft tissue, and characteristics of waterjet [51], [33], [34], [9] and [11]. Seok *et al.* [51] argued that the depth of jet penetration into cadaveric cheeks increases as the velocity, and pressure of the jet increases. Baxter *et al.* [11] showed that skin parameters such as Young's modulus play an important role in the skin penetration depth. They concluded that depth of penetration increases as the Young's modulus of skin decreases considering that the jet velocity, and nozzle diameter are kept constant. Our finding that DOC is almost linear with increasing waterjet velocity is in line with the results of Bahls *et al.* [9] that confirm that there is a linear relationship between waterjet pressure and DOC. This result is also consistent with the results of the depth of penetration of the high velocity projectile into soft tissue presented in [36], and the DOC of microject into gelatin vs. velocity of the microject presented in [57]. The effect of the modulus of elasticity on depth of penetration of the projectile is consistent with our results that as the modulus of elasticity increases, the depth of penetration decreases. Bahls *et al.* [9] also conducted some experiments with different combinations of gelatin and water, and found that the higher the ratio of the gelatin to water, the smaller the DOC. This is consistent with our finding that the DOC has an inverse relationship with the stiffness of the SEBS soft tissue simulants.

Equation (32) shows that the penetration pressure of waterjet increases as the diameter of the waterjet decreases, therefore there is an inverse relationship between penetration pressure and diameter of the waterjet. It also shows that penetration pressure has a direct relationship with fracture toughness, shear modulus, and strain hardening factor of the soft solid. (38) shows that depth of cut of waterjet in soft solid has a direct relationship with waterjet velocity and an inverse relationship with penetration pressure. These are in agreement with the experimental results depicted in [33] stating that DOC has a direct relationship with volumetric flow rate of the waterjet (thus the velocity of waterjet), and an inverse relationship with diameter of the waterjet, and stiffness of the soft solid. Although decreasing diameter increases the penetration pressure, however, according to (12) as diameter of the waterjet decreases the velocity of the waterjet increases and this increase is more than the increase in penetration pressure. Thus, the overall impact of decreasing diameter is the increase of DOC.

The shape of the stress-strain curve presented in Fig. 13, and 14 is consistent with the findings of the Shergold *et al.* [55] who measured the uniaxial stress vs. strain response of pig skin and silicone rubber at low and high strain rates (in the range of 0.004 to 4000 s^{-1}). It is also demonstrated that the common Mooney-Rivlin model is not suitable to describe the constitutive behavior of rubber-like solids, and Ogden strain energy density function is

a better option to describe the constitutive response of the soft solids with strong strain hardening capacity. According to their results, the constitutive response of pig skin is sensitive over the range of 0.004 to 4000 s^{-1}, but the silicone rubber stiffens and strengthens at strain rates over 40 s^{-1}. A similar trend is observed between the results of Shergold *et al.* [55] and our results. The stress level is increased by increasing the strain rate, but the shape of the constitutive response is unchanged. Similarly to this research, our results also consider that the strain hardening factor α does not change with strain rate, however increasing strain rates increase the shear modulus μ of the soft solid. The stiffening of the soft tissue while applying waterjet is also observed in the researches like [64]. In this research, authors observed that the colon wall was thickened by more than three times after application of the waterjet device.

The strain rate dependency of human tissues are explored in different studies. For instance Comley *et al.* [15] argued that adipose tissue has a Young's modulus of approximately $E = 1$kPa at low rates of strain on the order of 0.001 s^{-1}, and goes through a considerable stiffening with Young's modulus of $E = 3$ MPa at high rates of strain on the order of 1000 s^{-1}. This is in line with our results presented in Fig. 14.

According to several studies [10], and [55], the stress-strain curve of the soft tissue response is J-shaped, and that it is also strain rate dependent. The Ogden fit [40] is proved to be a good model to describe the constitutive response of materials that go through strain hardening like soft tissues. The Ogden model is good for incompressible, isotropic, and hyperelastic materials. The selected model for soft tissue assumed nonlinear elastic behavior whereas viscoelastic effects can also be present. The fact that the mechanical properties of the SEBS soft tissue simulants are strain rate sensitive implies the presence of viscoelastic effects over high rates of strain. SEBS is chosen as the main material for soft tissue simulants for model verification because of its viscoelastic nature that could mimic the response of real biological tissues while going through failure [36].

This research is done in line with developing motion models for a new class of steerable needles called Fracture-directed waterjet steerable needles [7], [66] and [8], in which the direction of tissue fracture is controlled by waterjet and then the flexible needle follows the path. Fig. 21 depicts the idea of fracture-directed waterjet steerable needles. Predicting DOC of waterjet in soft tissue is the first step towards developing control-friendly motion models for this class of steerable needles.

5 Conclusion and Future Work

In this paper, a mechanics-based model is proposed to predict the depth of cut of waterjet in soft tissue. The model can predict the DOC of waterjet in soft tissue based on tissue properties (constitutive response, and fracture toughness), and waterjet properties (velocity, and diameter). The model is verified with experiments in SEBS soft tissue simulants. This research sets

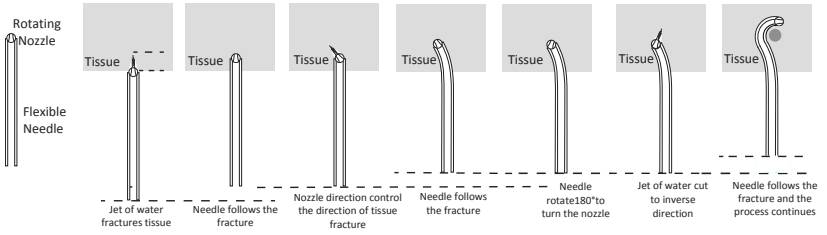

Fig. 21 New class of needle steering techniques namely fracture-directed waterjet needle steering. In this method, the direction of the tissue fracture is controlled by controllable waterjet nozzle, and then the flexible needle made of Nitinol follows the cut path by waterjet. This process continues until the needle reaches to the desired location in the soft tissue to perform the designated task either surgical or drug delivery. The direction of the needle can be controlled by rotating the nozzle inside the tissue, and cutting a new path in another direction by waterjet.

foundation to predict the depth-of-cut of waterjet in soft tissue for waterjet-assisted medical applications including waterjet surgery, and waterjet steerable needles. Future work include verifying the model with experiments in real biological tissues.

Appendix A: Procedure for Derivation of (27), and (28)

In this appendix, the procedure for derivation of the (27), and (28) is explained.

Equation (26) can be re-written using the volume change elements as:

$$\frac{\partial E_e}{\partial l_1} = \int_{r_1}^{\infty} \phi\, 2\pi s_1\, ds_1 = \int_{r_2}^{\infty} \phi\, 2\pi s_2\, ds_2 \tag{51}$$

Starting with $\int_{r_2}^{\infty} \phi\, 2\pi s_2\, ds_2$, and incorporating equation (25) one can write:

$$\int_{r_2}^{\infty} \phi\, 2\pi s_2\, ds_2 = \int_{r_2}^{\infty} 2\pi s_2 \frac{2\mu}{\alpha^2} \left[\left(\frac{s_1}{s_2}\right)^{\alpha} + \left(\frac{s_2}{s_1}\right)^{\alpha} - 2 \right] ds_2 \tag{52}$$

In order to make this integral neater, we can define: $\gamma = (\frac{s_2}{r_2})^2$, and thus $d\gamma = \frac{1}{{r_2}^2}(2s_2 ds_2)$. Therefore:

$$\begin{aligned} \frac{\partial E_e}{\partial l_1} = \int_{r_2}^{\infty} \pi {r_2}^2 \frac{2\mu}{\alpha^2} \left[\left(\frac{s_1}{s_2}\right)^{\alpha} + \left(\frac{s_2}{s_1}\right)^{\alpha} - 2 \right] \frac{2s_2}{{r_2}^2}\, ds_2 = \\ \int_{1}^{\infty} \pi {r_2}^2 \frac{2\mu}{\alpha^2} \left[\left(\frac{s_1}{s_2}\right)^{\alpha} + \left(\frac{s_2}{s_1}\right)^{\alpha} - 2 \right] d\gamma = \\ \frac{2\pi\mu {r_2}^2}{\alpha^2} \int_{1}^{\infty} \left[\left(\frac{s_1}{s_2}\right)^{\alpha} + \left(\frac{s_2}{s_1}\right)^{\gamma} - 2 \right] d\gamma \end{aligned} \tag{53}$$

$(\frac{s_1}{s_2})^\alpha$, and $\frac{s_2}{s_1})^\alpha$ can be re-written as:

$$\left(\frac{s_1}{s_2}\right)^\alpha = \frac{{s_1}^\alpha}{({s_2}^2)^{\frac{\alpha}{2}}} = \frac{{s_1}^\alpha}{(\gamma {r_2}^2)^{\frac{\alpha}{2}}} = \frac{{s_1}^\alpha}{\gamma^{\frac{\alpha}{2}} {r_2}^\alpha} \tag{54}$$

Using the same procedure, $(\frac{s_2}{s_1})^\alpha = \frac{\gamma^{\frac{\alpha}{2}} {r_2}^\alpha}{{s_1}^\alpha}$.

From volume conservation we already know that ${s_1}^2 - {r_1}^2 = {s_2}^2 - {r_2}^2$. Dividing the sides of this equation by ${r_2}^2$, we can write:

$$\frac{{s_1}^2 - {r_1}^2 + {r_2}^2}{{r_2}^2} = \left(\frac{s_2}{r_2}\right)^2 = \gamma \tag{55}$$

And thus:

$$\left(\frac{s_1}{r_2}\right)^2 = \left(\frac{r_1}{r_2}\right)^2 + \gamma - 1 = \left(\frac{d}{D}\right)^2 + \gamma - 1 \tag{56}$$

From here, the following equation can be deduced:

$$\begin{aligned} \left(\frac{s_1}{s_2}\right)^\alpha + \left(\frac{s_2}{s_1}\right)^\alpha - 2 = \\ \left(\frac{\gamma + (\frac{d}{D})^2 - 1}{\gamma}\right)^{\frac{\alpha}{2}} + \left(\frac{\gamma}{\gamma + (\frac{d}{D})^2 - 1}\right)^{\frac{\alpha}{2}} - 2 \\ \coloneqq f\left(\frac{d}{D}, \gamma\right) \end{aligned} \tag{57}$$

And thus (27), and (28) can be derived.

Acknowledgment

The authors would like to thank Alex Rodrigues and Sean Journot for their help in the experimental setup as well as Kraton Polymers LLC to provide samples of Kraton G1650, and G1652 for research.

References

1. Anderson, T.L.: Fracture mechanics: fundamentals and applications. CRC press (2017)
2. Arora, A., Hakim, I., Baxter, J., Rathnasingham, R., Srinivasan, R., Fletcher, D.A., Mitragotri, S.: Needle-free delivery of macromolecules across the skin by nanoliter-volume pulsed microjets. Proceedings of the National Academy of Sciences **104**(11), 4255–4260 (2007)
3. Aroussi, A.A., Sami, I.M., Leguerrier, A., Verhoye, J.P.: The blower: a useful tool to complete thrombectomy of the mechanical prosthetic valve. The Annals of thoracic surgery **81**(5), 1911–1912 (2006)
4. Asadian, A., Patel, R.V., Kermani, M.R.: Dynamics of translational friction in needle–tissue interaction during needle insertion. Annals of biomedical engineering **42**(1), 73–85 (2014)

5. Atkins, A.: Toughness and cutting: a new way of simultaneously determining ductile fracture toughness and strength. Engineering fracture mechanics **72**(6), 849–860 (2005)
6. Azar, T., Hayward, V.: Estimation of the fracture toughness of soft tissue from needle insertion. In: International Symposium on Biomedical Simulation, pp. 166–175. Springer (2008)
7. Babaiasl, M., Yang, F., Chen, Y., Ding, J.L., Swensen, J.P.: Predicting depth of cut of water-jet in soft tissue simulants based on finite element analysis with the application to fracture-directed water-jet steerable needles. In: 2019 International Symposium on Medical Robotics (ISMR), pp. 1–7. IEEE (2019)
8. Babaiasl, M., Yang, F., Swensen, J.P.: Towards water-jet steerable needles. In: 2018 7th IEEE International Conference on Biomedical Robotics and Biomechatronics (Biorob), pp. 601–608. IEEE (2018)
9. Bahls, T., Fröhlich, F.A., Hellings, A., Deutschmann, B., Albu-Schäffer, A.O.: Extending the capability of using a waterjet in surgical interventions by the use of robotics. IEEE Transactions on Biomedical Engineering **64**(2), 284–294 (2016)
10. Barnett, A.C., Lee, Y.S., Moore, J.Z.: Fracture mechanics model of needle cutting tissue. Journal of Manufacturing Science and Engineering **138**(1), 011005 (2016)
11. Baxter, J., Mitragotri, S.: Jet-induced skin puncture and its impact on needle-free jet injections: experimental studies and a predictive model. Journal of Controlled release **106**(3), 361–373 (2005)
12. Caputo, W.J., Beggs, D.J., DeFede, J.L., Simm, L., Dharma, H.: A prospective randomised controlled clinical trial comparing hydrosurgery debridement with conventional surgical debridement in lower extremity ulcers. International wound journal **5**(2), 288–294 (2008)
13. Chang, Y.C., Chen, Y., Ning, J., Cheng, H., Rock, M., Amer, M., Feng, S., Falahati, M., Wang, L.J., Chen, R.K.R., et al.: No such thing as trash: A 3d printable polymer composite comprised of oil extracted spent coffee grounds and polylactic acid with enhanced impact toughness. ACS Sustainable Chemistry & Engineering (2019)
14. Chua, B., Desai, S.P., Tierney, M.J., Tamada, J.A., Jina, A.N.: Effect of microneedles shape on skin penetration and minimally invasive continuous glucose monitoring in vivo. Sensors and Actuators A: Physical **203**, 373–381 (2013)
15. Comley, K., Fleck, N.: Deep penetration and liquid injection into adipose tissue. Journal of Mechanics of Materials and Structures **6**(1), 127–140 (2011)
16. den Dunnen, S., Dankelman, J., Kerkhoffs, G.M., Tuijthof, G.J.: How do jet time, pressure and bone volume fraction influence the drilling depth when waterjet drilling in porcine bone? Journal of the mechanical behavior of biomedical materials **62**, 495–503 (2016)
17. den Dunnen, S., Mulder, L., Kerkhoffs, G.M., Dankelman, J., Tuijthof, G.J.: Waterjet drilling in porcine bone: The effect of the nozzle diameter and bone architecture on the hole dimensions. Journal of the mechanical behavior of biomedical materials **27**, 84–93 (2013)
18. El-Domiaty, A., Abdel-Rahman, A.: Fracture mechanics-based model of abrasive water-jet cutting for brittle materials. The international journal of advanced manufacturing technology **13**(3), 172–181 (1997)
19. Falahati, M., Zhou, W., Yi, A., Li, L.: Fabrication of polymeric lenses using magnetic liquid molds. Applied Physics Letters **114**(20), 203701 (2019)
20. Falahati, M., Zhou, W., Yi, A., Li, L.: Development of an adjustable-focus ferrogel mirror. Optics & Laser Technology **125**, 106021 (2020)
21. Granick, M.S., Posnett, J., Jacoby BS, M., Noruthun, S., Ganchi, P.A., Datiashvili, R.O.: Efficacy and cost-effectiveness of a high-powered parallel waterjet for wound debridement. Wound repair and regeneration **14**(4), 394–397 (2006)
22. Hu, Y., Liu, T., Ding, J., Zhong, W.: Behavior of high density polyethylene and its nanocomposites under static and dynamic compression loadings. Polymer Composites **34**(3), 417–425 (2013)
23. Kaehler, G., Sold, M., Fischer, K., Post, S., Enderle, M.: Selective fluid cushion in the submucosal layer by water jet: advantage for endoscopic mucosal resection. European Surgical Research **39**(2), 93–97 (2007)

24. Kok, A.C., den Dunnen, S., Lambers, K.T., Kerkhoffs, G.M., Tuijthof, G.J.: Feasibility study to determine if microfracture surgery using water jet drilling is potentially safe for talar chondral defects in a caprine model. Cartilage p. 1947603519880332 (2019)
25. Kundu, P.K., Cohen, I.M.: Fluid mechanics 4th ed. Academic Press San Diego, CA (2008)
26. Liu, D., Zhu, H., Huang, C., Wang, J., Yao, P.: Prediction model of depth of penetration for alumina ceramics turned by abrasive waterjet—finite element method and experimental study. The International Journal of Advanced Manufacturing Technology **87**(9-12), 2673–2682 (2016)
27. Liu, J., Bai, Y., Xu, C.: Evaluation of ductile fracture models in finite element simulation of metal cutting processes. Journal of Manufacturing Science and Engineering **136**(1), 011010 (2014)
28. Liu, J., Ko, J.H., Secretov, E., Huang, E., Chukwu, C., West, J., Piserchia, K., Galiano, R.D.: Comparing the hydrosurgery system to conventional debridement techniques for the treatment of delayed healing wounds: a prospective, randomised clinical trial to investigate clinical efficacy and cost-effectiveness. International wound journal **12**(4), 456–461 (2015)
29. Mahvash, M., Hayward, V.: Haptic rendering of cutting: A fracture mechanics approach (2001)
30. Misra, S., Reed, K.B., Douglas, A.S., Ramesh, K., Okamura, A.M.: Needle-tissue interaction forces for bevel-tip steerable needles. In: Biomedical Robotics and Biomechatronics, 2008. BioRob 2008. 2nd IEEE RAS & EMBS International Conference on, pp. 224–231. IEEE (2008)
31. Misra, S., Reed, K.B., Schafer, B.W., Ramesh, K., Okamura, A.M.: Mechanics of flexible needles robotically steered through soft tissue. The International journal of robotics research **29**(13), 1640–1660 (2010)
32. Mitragotri, S.: Current status and future prospects of needle-free liquid jet injectors. Nature reviews Drug discovery **5**(7), 543 (2006)
33. Morad, S., Ulbricht, C., Harkin, P., Chan, J., Parker, K., Vaidyanathan, R.: Flexible robotic device for spinal surgery. In: 2014 IEEE International Conference on Robotics and Biomimetics (ROBIO 2014), pp. 235–240. IEEE (2014)
34. Morad, S., Ulbricht, C., Harkin, P., Chan, J., Parker, K., Vaidyanathan, R.: Modelling and control of a water jet cutting probe for flexible surgical robot. In: 2015 IEEE International Conference on Automation Science and Engineering (CASE), pp. 1159–1164. IEEE (2015)
35. Moradiafrapoli, M., Marston, J.: High-speed video investigation of jet dynamics from narrow orifices for needle-free injection. Chemical Engineering Research and Design **117**, 110–121 (2017)
36. Mrozek, R.A., Leighliter, B., Gold, C.S., Beringer, I.R., Jian, H.Y., VanLandingham, M.R., Moy, P., Foster, M.H., Lenhart, J.L.: The relationship between mechanical properties and ballistic penetration depth in a viscoelastic gel. Journal of the mechanical behavior of biomedical materials **44**, 109–120 (2015)
37. Oertel, J., Gaab, M.R., Knapp, A., Essig, H., Warzok, R., Piek, J.: Water jet dissection in neurosurgery: experimental results in the porcine cadaveric brain. Neurosurgery **52**(1), 153–159 (2003)
38. Oertel, J., Gaab, M.R., Warzok, R., Piek, J.: Waterjet dissection in the brain: review of the experimental and clinical data with special reference to meningioma surgery. Neurosurgical review **26**(26-4), 168–174 (2003)
39. Oertel, J., Gen, M., Krauss, J.K., Zumkeller, M., Gaab, M.R.: The use of waterjet dissection in endoscopic neurosurgery. Journal of neurosurgery **105**(6), 928–931 (2006)
40. Ogden, R., Saccomandi, G., Sgura, I.: Fitting hyperelastic models to experimental data. Computational Mechanics **34**(6), 484–502 (2004)
41. Ogden, R.W.: Large deformation isotropic elasticity–on the correlation of theory and experiment for incompressible rubberlike solids. Proceedings of the Royal Society of London. A. Mathematical and Physical Sciences **326**(1567), 565–584 (1972)
42. Oh, T.M., Cho, G.C.: Rock cutting depth model based on kinetic energy of abrasive waterjet. Rock Mechanics and Rock Engineering **49**(3), 1059–1072 (2016)

43. Orlowski, K.A., Ochrymiuk, T., Atkins, A., Chuchala, D.: Application of fracture mechanics for energetic effects predictions while wood sawing. Wood Science and Technology **47**(5), 949–963 (2013)
44. Rau, H., Duessel, A., Wurzbacher, S.: The use of water-jet dissection in open and laparoscopic liver resection. HPB **10**(4), 275–280 (2008)
45. Rau, H., Meyer, G., Jauch, K., Cohnert, T., Buttler, E., Schildberg, F.: Liver resection with the water jet: conventional and laparoscopic surgery. Der Chirurg; Zeitschrift fur alle Gebiete der operativen Medizen **67**(5), 546–551 (1996)
46. Roesthuis, R.J., van de Berg, N.J., van den Dobbelsteen, J.J., Misra, S.: Modeling and steering of a novel actuated-tip needle through a soft-tissue simulant using fiber bragg grating sensors. In: Robotics and Automation (ICRA), 2015 IEEE International Conference on, pp. 2283–2289. IEEE (2015)
47. Römgens, A.M., Rem-Bronneberg, D., Kassies, R., Hijlkema, M., Bader, D.L., Oomens, C.W., van Bruggen, M.P.: Penetration and delivery characteristics of repetitive microjet injection into the skin. Journal of controlled release **234**, 98–103 (2016)
48. Sato, C., Nakano, T., Nakagawa, A., Yamada, M., Yamamoto, H., Kamei, T., Miyata, G., Sato, A., Fujishima, F., Nakai, M., et al.: Experimental application of pulsed laser-induced water jet for endoscopic submucosal dissection: Mechanical investigation and preliminary experiment in swine. Digestive Endoscopy **25**(3), 255–263 (2013)
49. Schramm-Baxter, J., Katrencik, J., Mitragotri, S.: Jet injection into polyacrylamide gels: investigation of jet injection mechanics. Journal of biomechanics **37**(8), 1181–1188 (2004)
50. Schramm-Baxter, J., Mitragotri, S.: Needle-free jet injections: dependence of jet penetration and dispersion in the skin on jet power. Journal of Controlled Release **97**(3), 527–535 (2004)
51. Seok, J., Oh, C.T., Kwon, H.J., Kwon, T.R., Choi, E.J., Choi, S.Y., Mun, S.K., Han, S.H., Kim, B.J., Kim, M.N.: Investigating skin penetration depth and shape following needle-free injection at different pressures: A cadaveric study. Lasers in surgery and medicine **48**(6), 624–628 (2016)
52. Seto, T., Yamamoto, H., Takayama, K., Nakagawa, A., Tominaga, T.: Characteristics of an actuator-driven pulsed water jet generator to dissecting soft tissue. Review of Scientific Instruments **82**(5), 055105 (2011)
53. Shergold, O.A., Fleck, N.A.: Mechanisms of deep penetration of soft solids, with application to the injection and wounding of skin. Proceedings of the Royal Society of London. Series A: Mathematical, Physical and Engineering Sciences **460**(2050), 3037–3058 (2004)
54. Shergold, O.A., Fleck, N.A., King, T.S.: The penetration of a soft solid by a liquid jet, with application to the administration of a needle-free injection. Journal of biomechanics **39**(14), 2593–2602 (2006)
55. Shergold, O.A., Fleck, N.A., Radford, D.: The uniaxial stress versus strain response of pig skin and silicone rubber at low and high strain rates. International Journal of Impact Engineering **32**(9), 1384–1402 (2006)
56. Shi, H., Jiang, S.J., Li, B., Fu, D.K., Xin, P., Wang, Y.G.: Natural orifice transluminal endoscopic wedge hepatic resection with a water-jet hybrid knife in a non-survival porcine model. World Journal of Gastroenterology: WJG **17**(7), 926 (2011)
57. Tagawa, Y., Oudalov, N., El Ghalbzouri, A., Sun, C., Lohse, D.: Needle-free injection into skin and soft matter with highly focused microjets. Lab on a Chip **13**(7), 1357–1363 (2013)
58. Tschan, C., Tschan, K., Krauss, J., Oertel, J.: First experimental results with a new waterjet dissector: Erbejet 2. Acta neurochirurgica **151**(11), 1473–1482 (2009)
59. Vollmer, C.M., Dixon, E., Sahajpal, A., Cattral, M.S., Grant, D.R., Gallinger, S., Taylor, B.R., Greig, P.D.: Water-jet dissection for parenchymal division during hepatectomy. HPB **8**(5), 377–385 (2006)
60. Wang, J.: Predictive depth of jet penetration models for abrasive waterjet cutting of alumina ceramics. International Journal of Mechanical Sciences **49**(3), 306–316 (2007)
61. Wang, J.: A new model for predicting the depth of cut in abrasive waterjet contouring of alumina ceramics. Journal of materials processing technology **209**(5), 2314–2320 (2009)

62. Wang, J., Guo, D.: A predictive depth of penetration model for abrasive waterjet cutting of polymer matrix composites. Journal of materials processing technology **121**(2-3), 390–394 (2002)
63. Wilkins, R., Graham, E.: An erosion model for waterjet cutting. Journal of engineering for industry **115**(1), 57–61 (1993)
64. Yahagi, N., Neuhaus, H., Schumacher, B., Neugebauer, A., Kaehler, G., Schenk, M., Fischer, K., Fujishiro, M., Enderle, M.: Comparison of standard endoscopic submucosal dissection (esd) versus an optimized esd technique for the colon: an animal study. Endoscopy **41**(04), 340–345 (2009)
65. Yamada, M., Nakano, T., Sato, C., Nakagawa, A., Fujishima, F., Kawagishi, N., Nakanishi, C., Sakurai, T., Miyata, G., Tominaga, T., et al.: The dissection profile and mechanism of tissue-selective dissection of the piezo actuator-driven pulsed water jet as a surgical instrument: Laboratory investigation using swine liver. European Surgical Research **53**(1-4), 61–72 (2014)
66. Yang, F., Babaiasl, M., Swensen, J.P.: Fracture-directed steerable needles. Journal of Medical Robotics Research **4**(01), 1842002 (2019)
67. Yoshimi Tanaka Rikimaru Kuwabara, Y.H.N.T.K.J.P.G., Osada, Y.: Determination of fracture energy of high strength double network hydrogels. The Journal of Physical Chemistry B **109**, 11559–11562 (2005)

Author biography

Mahdieh Babaiasl received her M.S. degree in Mechatronics Engineering from the University of Tabriz, Iran. From 2011 to 2013, she was at the University of Tabriz as Research Assistant at Mechatronics laboratory. As a research assistant at university of Tabriz, she designed and controlled an exoskeleton robot for upper-limb rehabilitation and a surgical robot. She serves as a reviewer for several prestigious journals and conferences including MBEC, IEEE access, TIMC, and COMPELECENG among others. She is currently a Research Assistant in the Department of Mechanical Engineering, Washington State University, USA under the supervision of Dr. John P. Swensen. Her research interests are steerable needles, water-jet assisted medical applications, and medical devices.

Stefano Boccelli graduated in aerospace engineering (BSc, 2013) and aeronautical engineering (MSc, 2016) from Politecnico di Milano with a thesis on the modeling of chemically reacting flows. Subsequently, he joined the Research Master program (ex Diploma Course) of the von Karman Institute

for Fluid Dynamics, working on the simulation of high Mach number rafefied flows. He is currently a PhD candidate in Politecnico di Milano, focusing on computer modeling of Hall thruster devices. His research interests include hypersonic non-equilibrium flows, plasma physics and fluid mechanics.

Yao Chen received his M.S. degree in Mechanical Engineering from University of Southern California in 2013. He continued his Ph.D. study at Washington State University. His research interest is in the mechanical behaviors of polymer composites.

Fan Yang received his B.S. in Mechanical Engi- neering from the Shanghai Institute of Tech- nology. He is currently pursuing his Ph.D. degree in the Department of Mechanical Engi- neering at Washington State University. He is a graduate research assistant in the Modeling, Motion, and Medical (M3) Robotics Laboratory under the supervision of Dr. John P. Swensen. His research interests include steerable needles, continuum robotics, and medical devices.

Jow-Lian Ding is a Professor in the School of Mechanical and Materials Engineering at Washington State University. He obtained his PhD degree in solid mechanics from Brown University in 1983. His research interests are in the areas of mechanics of materials, materials science, dynamic responses of

materials and structures, and shock physics. He held visiting appointments at Oak Ridge National Laboratory in1990 and Sandia National Laboratories, Albuquerque in 2000. Dr. Ding is a Fellow of American Society of Mechanical Engineers (ASME).

John P. Swensen received his M.S. and Ph.D. degrees in Mechanical Engineering from the the Johns Hopkins University, U.S.A, in 2009 and 2012, respectively. He is currently an Assistant Professor in the School of Mechanical and Materials Engineering at Washington State University, and the Director of the Modeling, Motion, and Medical (M3) Robotics Laboratory. The M3 Robotics Laboratory research focuses on research into compliant medical devices, including steerable needles, and other tunably-compliant mechanisms.